A neurite-zippering mechanism, mediated by layer-specific expression of IgCAMs, regulates synaptic laminar specificity in the *C. elegans* nerve ring neuropil

Authors: Titas Sengupta[1], Noelle L. Koonce[1], Mark W. Moyle[1], Leighton H. Duncan[1], Nabor Vázquez-Martínez[1], Xiaofei Han[2], Lin Shao[1], Yicong Wu[2], Anthony Santella[3], Li Fan[3], Zhirong Bao[3], William A. Mohler[5], Hari Shroff[2, 4], Daniel A. Colón-Ramos[1, 4, 6*]

Affiliations:

1. Department of Neuroscience and Department of Cell Biology, Yale University School of Medicine, New Haven, CT 06536, USA.

2. Laboratory of High Resolution Optical Imaging, National Institute of Biomedical Imaging and Bioengineering, National Institutes of Health, Bethesda, MD 20892, USA.

3. Developmental Biology Program, Sloan Kettering Institute, New York, NY 10065, USA.

4. MBL Fellows, Marine Biological Laboratory, Woods Hole, MA 02543, USA

5. Department of Genetics and Genome Sciences and Center for Cell Analysis and Modeling, University of Connecticut Health Center, Farmington, CT 06030, USA.

6. Instituto de Neurobiología, Recinto de Ciencias Médicas, Universidad de Puerto Rico, San Juan 00901, Puerto Rico. 56

*Correspondence to:

Daniel A. Colón-Ramos, Ph.D.
Department of Neuroscience
Department of Cell Biology
Yale University School of Medicine
333 Cedar Street
SHM B 163D
New Haven, CT 06510
Email: daniel.colon-ramos@yale.edu

Abstract

A fundamental design principle of nervous systems is the grouping of neuronal contacts into layers within nerve bundles. The layered arrangement of neurites requires nanoscale precision in their placement within bundles, and this precision, which can not be exclusively explained by simple tip-directed outgrowth dynamics, underpins synaptic specificity and circuit architecture. Here we implement novel imaging methods and deep learning approaches to document the specific placement of single neurites during the assembly of the *C. elegans* nerve ring. We uncover a zippering mechanism that controls precise placement of neurites onto specific layer subdomains. Nanoscale precision in neurite placement is orchestrated via temporally-regulated expression of specific Ig adhesion molecules, such as SYG-1. Ig adhesion molecules act as instructive signals, defining sublaminar regions and guiding neurite zippering onto target neurons. Our study reveals novel developmental mechanisms that coordinate neurite placement and synaptic specificity within layered brain structures.

Introduction

In brains, neurites are segregated away from the cell bodies into synapse-rich regions termed neuropils: dense structures of nerve cell extensions which commingle to form functional circuits (Maynard, 1962). Neuropils are units of functional organization within brains, and within the precisely arranged architecture of the neuropil, placement of neurites into specific neighborhoods is a major determinant of synaptic specificity and circuit connectivity (Maynard, 1962; Schürmann, 2016; Soiza-Reilly & Commons, 2014; Xu et al., 2020; Zheng et al., 2018). Proper functional connectivity therefore depends on design principles that guide placement of neurites, at nanoscale precision, within neuropils.

A fundamental design principle of neuropil organization is the segregation of neurites into laminae and sublaminae, and this laminar organization principle is conserved and observed in neuropils of both vertebrate and invertebrates (Gabriel et al., 2012; Millard & Pecot, 2018; Sanes & Zipursky, 2010). The laminar structural organization is key to the assembly and functional segregation of specific circuits (Gabriel et al., 2012; Kolodkin & Hiesinger, 2017; Millard & Pecot, 2018; Nevin et al., 2008). For example, in the inner plexiform layer (IPL) of the vertebrate retina, synaptic connections conveying different types of visual information spatially segregate onto distinct sublayers. Placement of neurites with similar functions into specific sublayers restricts synaptic partner choice, driving synaptic specificity (Robles et al., 2013). Therefore, the co-segregation of neurons with similar response properties into specific layers gives rise to topographic maps in which structural principles underpin functional

73 principles in the precise assembly, and segregation, of distinct circuits (Clandinin &
74 Feldheim, 2009).

75 Within the layered organization of neuropils, subsets of neurons are capable of
76 specifically projecting onto multiple layers, enabling integration of information across
77 laminar circuits. For example, glycinergic and GABAergic amacrine cells in the IPL of
78 the retina, and the periventricular projection neurons in the zebrafish tectal neuropil,
79 extend single neurites that link multiple sublayers within their respective neuropils
80 (Demb & Singer, 2012; Kolb, 1995; Kunzevitzky et al., 2013; Robles et al., 2011; Strettoi
81 et al., 1992; Taylor & Smith, 2012). Their precise placement, and the distribution of
82 synapses within neurite regions, underlies their functional roles as integrators of
83 information across the modular and layered circuit architecture (Robles et al., 2011;
84 Strettoi et al., 1992; Taylor & Smith, 2012). How the precise placement of these
85 multilayer-spanning neurites is specified during development, particularly in the context
86 of the assembling neuropil, is not understood.

87 Molecular genetic studies have revealed roles for cell adhesion molecules
88 (CAMs) and guidance factors in neuronal targeting onto specific layers of the brain. For
89 example, studies in both the mouse and fly visual systems have revealed important
90 roles for IgSF proteins, such as the Sidekick, Dscam and Contactin molecules, in
91 targeting neurons to distinct layers or sublaminae (Sanes & Zipursky, 2020; Tan et al.,
92 2015; Yamagata & Sanes, 2008, 2012). These studies indicate that the expression
93 levels, the timing of expression and the co-expression of specific CAMs influence layer-
94 specific targeting of neurites within neuropils (Petrovic & Hummel, 2008a; Poskanzer et
95 al., 2003; Schwabe et al., 2014). These observations also reveal that our current

96 mechanistic frameworks of axon guidance and cell-cell interactions are insufficient to
97 provide a conceptual understanding of how nanoscale organization within neuropils
98 emerges during development. In particular, how single cells make simultaneous and
99 coordinated use of these molecular cues to achieve precise placement, resulting in
100 synaptic specificity within layered neuropils, is poorly understood.

101 The *C. elegans* nerve ring is a crowded neuropil tens of micrometers thick in
102 which neuronal processes have to discriminate between targets to assemble functional
103 circuits that underpin specific behaviors (Ware et al., 1975; White et al., 1986). We
104 recently demonstrated that the *C. elegans* nerve ring neuropil is a layered structure,
105 with layers (called "strata") that functionally segregate sensory information and motor
106 outputs (Moyle et al., 2020). A subset of highly interconnected neurons, which form part
107 of a group called 'rich-club neurons', serve as hubs that link functionally distinct strata,
108 analogous to amacrine cells in the inner plexiform layer of the vertebrate retina (Marc et
109 al., 2014; Moyle et al., 2020; Towlson et al., 2013). The precise placement of these rich-
110 club neurons along distinct nerve ring strata, and the specific segregation of their
111 synaptic inputs and outputs between these strata, are important for supporting the
112 structure and function of the nematode brain (Gray et al., 2005; Moyle et al., 2020;
113 Wakabayashi et al., 2004).

114 To determine how neuronal processes are precisely placed onto specific layers
115 during development, and the implications of this placement for synaptic connectivity, we
116 examined the AIB interneurons, a pair of "rich-club neurons" that integrate sensory and
117 motor information across nerve ring strata (Chalasani et al., 2007; Kang & Avery, 2009;
118 Moyle et al., 2020; Sabrin et al., 2019; Towlson et al., 2013). Each AIB neuron projects

119 a single neurite, and segments of that single neurite are placed along distinct and
120 specific layers in the *C. elegans* nerve ring. The nanoscale precision of AIB neurite
121 placement informs the specificity of AIB synaptic sites in the dense neuropil structure of
122 the nerve ring.

123 We labeled the AIB neurons for visualization *in vivo* and implemented novel
124 imaging methods and deep learning approaches to yield high-resolution images of AIB
125 during embryonic development. We discovered that placement of the AIB neurite
126 depends on coordinated zippering mechanisms that align segments of the AIB neurite
127 onto specific sublayers. Through forward and reverse genetic screens we uncovered
128 molecular factors important for placement of the AIB neurite. We identified roles for the
129 IgCAM *syg-1* in zippering a segment of the AIB neurite onto a layer boundary. We
130 determined that *syg-1* expression is layer specific, and temporally controlled to coincide
131 with AIB neurite outgrowth and zippering onto the correct sublayer. Expression of SYG-
132 1 is sufficient to specify AIB neurite placement, and ectopic expression of just the SYG-
133 1 ectodomain results in segments of the AIB neurite being incorrectly positioned at the
134 ectopic SYG-1-expressing layers. Our findings uncover a novel zippering mechanism
135 which acts *in vivo* to place neurites along specific layers of the nerve ring neuropil. This
136 mechanism is based on a temporally-coordinated expression of IgCAMs at specific
137 layer subdomains. The developmental processes uncovered in this *in vivo* study might
138 represent conserved mechanisms that enable placement of neurites, and *en passant*
139 synaptic specificity, in layered neuropil structures.

140

141

142 **Results**

143

144 **The AIB neurites are placed along distinct strata in the *C. elegans* nerve**

145 **ring neuropil**

146 To characterize the precise placement and synaptic distribution of the AIB neurites in
147 the context of the nerve ring neuropil strata, we examined available connectome
148 datasets generated across the larval developmental stages of *C. elegans*(White et al.,
149 1986; Witvliet et al., 2020). Synapses in AIB, like in most nerve ring neurons, are
150 formed *en passant*, or along the length of its single neurite. AIB displays polarity in the
151 distribution of its synaptic specializations: postsynaptic specializations are enriched in
152 the proximal neurite (near the cell body), while presynaptic specializations are enriched
153 in the distal neurite (Fig. 1a-c). Examination of the connectomes revealed that the
154 synaptic polarity of AIB is stereotyped, established by the L1 stage and preserved
155 throughout development (Witvliet et al., 2020)(https://nemanode.org/).

156 Segments of the AIB single neurite reside along distinct strata of the nerve ring
157 (Supplementary Fig. 1a). The AIB proximal neurite, which is enriched in postsynaptic
158 specializations, forms contacts with neighboring amphid sensory neurons in a sub-
159 bundle coincident with S3/S4 sublaminar region, hereafter termed 'AIB proximal
160 neighborhood'. The AIB distal neurite, which is enriched in presynaptic specializations,
161 contacts neighboring motor interneurons in a sub-bundle coincident with S2/S3
162 sublaminar region, hereafter termed 'AIB distal neighborhood'. In the distal
163 neighborhood, the highest number of AIB contacts are formed with the neurites of motor
164 neuron RIM (Supplementary Fig. 1b,c), a major fasciculation partner and postsynaptic

165 partner of AIB, located at the S2/S3 sublaminar region (Supplementary Fig. 1b). In the
166 proximal neighborhood, AIB receives synaptic inputs from sensory neurons in the S3/4
167 sublaminar region (Supplementary Fig. 1b,d). Therefore, placement of the AIB neurite
168 onto these distinct neighborhoods links sensory information (from the S3/4 sublaminar
169 region) to motor neuron outputs (in the S2/S3 sublaminar region) in the nerve ring
170 neuropil. This design principle of the AIB neurite is present in early larval stages and
171 preserved upto adulthood (Supplementary Fig. 1b)(Witvliet et al., 2020).

172 The AIB neurite segments reach the proximal and distal neighborhoods via a
173 shift of the neurite along the anteroposterior axis, precisely at the dorsal mid-line of the
174 nerve ring (herein refered to as the “chiasm”, as the shift results in a cross-over of the
175 two AIB neurites; indicated by arrowheads in Fig.1a-g, Supplementary Fig. 1e-j).
176 Remarkably, the shift of the AIB neurite is precisely the width of the S3 strata, enabling
177 it to bridge the S3/4 and S2/3 sublaminae with the positioning of its neurite segments
178 (Supplementary Fig. 1). Network analyses on the contacts of AIBL and AIBR with other
179 neurons across the available connectomes revealed similarity in number and
180 distribution of AIB contacts across development (pairwise cosine similarity index S,
181 ranges from 0.62-0.97, S>0.5 representing a positive correlation between datasets,
182 Supplementary Fig. 2a-c also see Methods). This is indicative of a developmental
183 program that establishes contact profiles for AIB during embryogenesis, and is
184 allosterically maintained during post-embryonic growth (Fan et al., 2020). We also found
185 that AIBL and AIBR have high betweenness centrality (a standard property for rich-club
186 neurons (Towlson et al., 2013)) in an L1 (first larval stage after embryogenesis) and an
187 adult connectome dataset (Witvliet et al., 2020), suggesting that AIB functions as a rich

188 club neuron at early as well as later postembryonic developmental stages
189 (Supplementary Fig. 2d). Moreover, examination of AIB in the connectome of the
190 nematode *Pristionchus pacificus,* which is separated from *C. elegans* by 100 million
191 years of evolutionary time, revealed similar design principles in morphology and
192 placement of the AIB neurite (Hong et al., 2019). Therefore AIB morphology, position
193 and polarity are conserved features of the architecture of the nematode brain,
194 established during embryonic development and are uniquely designed to integrate and
195 relay information across functional modules of the nerve ring. The developmental
196 programs that govern these design principles, enabling nanoscale precision in the
197 placement of the AIB neurite onto specific neighborhoods and the segregation of
198 synaptic specializations, are not understood.
199

200 **_In vivo_ visualization of AIB synaptic distribution and placement in the nerve**
201 **ring neuropil**

202 To examine the developmental programs of AIB, we developed cellular and
203 subcellular fluorescent labels for imaging of AIB, its neighborhoods and its synapses *in*
204 *vivo* in embryonic stages and postembryonic larval stages. The synaptic distribution that
205 we observed by fluorescent labeling was consistent with the EM connectomic
206 characterizations: presynaptic proteins RAB-3 and CLA-1 localized exclusively to the
207 distal segment of the neurite, while postsynaptic protein GLR-1 localized primarily to the
208 proximal neurite segment (Fig. 1d,e; Polarity index, PI = 0.92 for RAB-3 and 0.24 for
209 GLR-1, where PI>0.5 represents a distal localization and PI<0.5 represents a proximal
210 localization). These markers also enable visualization of the chiasm that result in the

separation of the two AIB neurite segments onto distinct neighborhoods along the antero-posterior axis of the worm (Fig. 1f-l, Supplementary Fig. 1g,h). We found that the chiasm is stereotyped and similar in length across L4 stage animals, as measured from confocal micrographs (mean length = 2.97±0.22 μm, number of neurons measured, n =22), and electron micrographs (dorsal midline shift length in AIBL and AIBR in electron micrographs of an L4 stage animal, JSH, are 3.01 μm and 3.16 μm respectively).

To visualize the AIB neurite in the context of the proximal and distal neighborhoods, we co-labeled neurons that extensively contact (fasciculate) with AIB in the proximal and distal neighborhoods: motor neuron RIM for the distal neighborhood and sensory neurons AWC and ASE for the proximal neighborhood (Supplementary Fig. 1c,d). Consistent with the EM connectomic studies, these representative neighborhood markers overlap with the expected neighborhoods (Fig. 1f-m). Our findings are consistent with and extend previous studies, demonstrating that the AIB unique morphology emerges early in development, is stereotyped across animals and is conserved throughout evolution (Hong et al., 2019; White et al., 1983). Our examination of AIB in the context of electron micrographs from connectomic studies and *in vivo* imaging reveal that the AIB neurite is designed, by its position and distribution of synapses, to occupy distinct neighborhoods and integrate information across strata of the nerve ring.

233 **Modular developmental programs underlie precise placement and synaptic**
234 **polarity of the AIB neurites**

235 To understand the cellular and molecular mechanisms underpinning the precise
236 placement of the AIB neurites in the context of the nerve ring neuropil, and how their
237 placement relates to synaptic polarity, we performed unbiased forward genetic screens
238 and candidate screens in postembryonic larval stage animals. Our screens uncovered
239 mutants with defects in AIB neurite outgrowth and placement: a novel mutant allele of
240 transcription factor *daf-16*/FOXO (*ola337*) (Supplementary Table 1), lesions in genes
241 encoding cytoskeletal regulators (*unc-33 and zyg*-8) and lesions in axon guidance
242 genes (*vab-1*, *unc-6* and *sax-3)*. These mutants result in defects in AIB neurite
243 placement in the context of the neighborhoods by affecting AIB outgrowth and/or nerve
244 ring neighborhood development (Fig. 2; Supplementary Fig. 3), (Christensen et al.,
245 2011; Grossman et al., 2013; Yoshimura et al., 2008; Zallen et al., 1999)). Interestingly,
246 inspection of AIB subcellular distribution of pre- and postsynaptic specializations in
247 these mutant backgrounds revealed that when AIB morphology and the nerve ring
248 neighborhoods are affected, the AIB neurites still exhibit a polarized distribution of pre-
249 and postsynaptic proteins (Fig. 2). For instance, even in cases in which the distal AIB
250 neurite segment was largely absent, the neurite retained the polarized distribution of pre
251 and postsynaptic proteins, with presynaptic components accumulating specifically in the
252 distal segment, or tip, of the truncated neurite and not in the proximal neurite (Fig. 2e-l).
253 The retainment of synaptic polarity even in extreme cases of neurite outgrowth or
254 neighborhood placement defects suggests modularity between the developmental

255 processes dictating neurite placement and the polarized distribution of pre- and
256 postsynaptic specializations in the context of the proximal and distal neurite segments.
257 Our genetic findings suggest that synaptic specificity in AIB requires the correct
258 deployment of two modular developmental programs: polarized placement of pre- and
259 postsynaptic specializations along the neurite, and the placement of the neurite onto the
260 correct strata. To specifically understand the mechanisms that regulate placement of
261 the AIB neurite onto the correct strata, we focused our analyses on mutants with
262 nanoscale defects in the placement of the AIB neurite within specific neighborhoods.
263

264 **The IgCAM SYG-1 is required for precise placement of the AIB distal**
265 **neurite in the nerve ring**

266 From our screens we discovered that loss-of-function mutant alleles of the Ig
267 superfamily CAM gene *syg-1* result in significant defects in placement of the AIB neurite
268 in the nerve ring. In wild type animals, we observed overlap between the AIB distal
269 neurite, and its distal neighborhood partner, RIM (Fig. 3a-d), consistent with electron
270 microscopy characterizations of AIB and RIM fasciculation (Supplementary Fig. 1b). In
271 contrast, in *syg-1* mutants the AIB neurites are frequently detached or separated from
272 the RIM neurites (Fig. 3e-h). 70.7% of *syg-1(ky652)* animals and 62.5% of *syg-*
273 *1(ok3640)* animals (as compared to 0% of wild type animals) show regions of AIB-RIM
274 detachment, i.e., failure of the AIB and RIM neurites to fasciculate along their entire
275 length in the distal neighborhood. Cosmid C54A10, containing the *syg-1* genomic
276 region, rescued the distal neurite placement defects in *syg-1(ky652)* (in 87.5% of
277 animals with the rescuing construct, the AIB and RIM neurites show complete overlap

278 as in wild type animals) (Fig. 3i-l). In the *syg-1(ky652)* animals that exhibit defects in AIB
279 neurite placement with respect to RIM, we calculated the percentage of AIB-RIM neurite
280 contact length that exhibits detachment or separation, and found the average percent
281 detachment to be 21.49±4% of total contact length in *syg-1(ky652)* mutant animals (Fig.
282 1m, also see Methods). The AIB chiasm is also significantly reduced in length in *syg-1*
283 mutants (Supplementary Fig. 4a), and the distal neurite is not positioned at a uniform
284 distance from the proximal AIB neurite (Fig. 1n), consistent with a placement defect of
285 the AIB distal neurite onto the distal neighborhood . We note that in the *syg-1(ky652)*
286 mutant animals, the cell body position of AIB, AIB's neurite length and placement of the
287 AIB proximal neurite segment are unaffected (Supplementary Fig. 4b,c), suggesting that
288 *syg-1* specifically regulates the placement of the distal neurite segment in the distal
289 neighborhood. Our findings indicate that correct placement of the AIB proximal neurite
290 and the distal neurite are genetically separable. Importantly, our findings indicate that Ig
291 superfamily cell adhesion molecule SYG-1 is necessary for nanoscale placement of the
292 AIB neurite to the distal nerve ring neighborhood.

293 SYG-1 and its orthologs (Rst and Kirre in *Drosophila* and Kirrel1/2/3 in mammals)
294 are multipurpose adhesion molecules which function in a wide variety of developmental
295 contexts, including synapse formation in the *C. elegans* egg-laying circuit, muscle cell
296 fusion, eye patterning and olfactory axon convergence in *Drosophila*, and formation of
297 the kidney filtration barrier in mammals (S. Bao & Cagan, 2005; Garg et al., 2007; Kim
298 et al., 2015; Serizawa et al., 2006; Shen & Bargmann, 2003; ztokatli et al., 2012). Given
299 SYG-1's known role in synaptogenesis in *C. elegans*, we examined the distribution of
300 synaptic sites along the AIB distal neurite in *syg-1* mutants. We noted reduction in RAB-

301 3 signal in regions of the AIB distal neurite, but specifically for areas lacking RIM
302 contacts (Supplementary Fig. 4g-p). We hypothesized that SYG-1 could mediate
303 synaptogenesis in AIB, and that synapses might then help place AIB in the distal
304 neighborhood. To test this hypothesis we identified, from our forward and reverse
305 genetic screens, additional lesions resulting in synaptogenesis defects in AIB, including
306 a novel allele of *syd-2(ola341)* (Supplementary Table 1), and *cla-1(ok560)* (Barstead et
307 al., 2012; Xuan et al., 2017; Zhen & Jin, 1999). We observed that while *syd-2* and *cla-1*
308 mutants result in an abnormal distribution of presynaptic specializations in AIB
309 (Supplementary Fig. 4q-t), they do not display phenotypes in AIB neurite placement
310 within the distal neighborhood (Supplementary Fig. 4u). Our findings indicate that
311 molecules that affect synaptogenesis do not necessarily result in fasciulation defects for
312 AIB. Together, our findings suggest that SYG-1 plays a role in mediating neurite
313 placement specifically onto the distal neighborhood via fasciculation.
314

315 **RIM neurons express SYG-1 and regulate AIB neurite placement**

316 To understand how *syg-1* regulates the precise placement of the AIB neurite in its
317 distal neighborhood, we next investigated where the *syg-1* gene is expressed. We
318 achieved this by co-expressing an AIB reporter and a transcriptional reporter of *syg-1*
319 (Schwarz et al., 2009) and examining its expression in the nerve ring of wild type
320 animals. We observed robust expression of the *syg-1* transcriptional reporter in a
321 banded pattern in the nerve ring neuropil, with specific enrichment in the AIB proximal
322 and distal neighborhoods (Fig. 4a-d). By quantifying the ratio of mean intensities of the
323 *syg-1* reporter in the proximal and distal neighborhoods, we found that on average, *syg-*

324 *1* expression levels were 3.37 times (S.E.M. = 0.12) higher in the distal neighborhood
325 relative to the proximal neighborhood (Fig. 4i). We then tested whether RIM, the primary
326 distal neighborhood fasciculaton partner of AIB, expresses *syg-1*. Indeed, co-
327 localization studies revealed *syg-1* reporter expression in RIM, but not in AIB, consistent
328 with previous observations (Schwarz et al., 2009) (Fig. 4a-h). Therefore, neurons in the
329 AIB distal nerve ring neighborhood, including RIM, express SYG-1.

330 As *syg-1* mutant animals exhibit defects in AIB neurite placement in the distal
331 neighborhood, and as SYG-1 is expressed in RIM, we hypothesized that the RIM
332 neurons might regulate placement of the AIB distal neurite onto the distal neighborhood.
333 Via promoter screening and a systematic lineage tracing and cell identification pipeline
334 (Z. Bao et al., 2006; Boyle et al., 2006; Duncan et al., 2019; Murray et al., 2006;
335 Santella et al., 2014), we identified two promoters expressed in the RIM neurons prior to
336 embryonic growth and placement of the AIB distal neurite (which occurs approximately
337 520-570 m.p.f. – see next section and Fig. 5). The promoters identified were *inx-19p*
338 (expressed in RIM starting ~370 m.p.f (minutes post fertilization)) and *tdc-1p* (expressed
339 in RIM starting ~445 m.p.f) (see Methods, Supplementary Fig. 5),
340 http://promoters.wormguides.org). We then used these early promoters to drive an *in-*
341 *vivo* split caspase ablation system (Chelur & Chalfie, 2007) to successfully eliminate the
342 RIM neurons during embryogenesis (Supplementary Fig. 5d-g). Consistent with our
343 hypothesis, we observed that ablation of RIM results in defects in placement of the AIB
344 distal neurite to the distal neighborhood. These defects in RIM-ablated animals
345 phenocopy the defects seen for the *syg-1* mutants. 80.6% and 51.5% of animals had
346 defects in AIB distal neurite placement in RIM-ablated animals (using two strategies-

347 see Supplementary figure 5 and Methods), compared to 3.1% in a wild type population;
348 Fig. 4j-q). These observations demonstrate that SYG-1-expressing RIM neurons are
349 necessary for the precise placement of the AIB neurite in the distal neighborhood.
350

351 **The AIB neurite is positioned in the distal neighborhood during embryonic**
352 **development via a novel zippering mechanism**

353 To understand how the RIM neurons contribute to placement of the AIB distal
354 neurite segment, we examined the placement of the AIB and RIM neurites during
355 embryogenesis. Imaging AIB and RIM in embryos required integration of subtractive
356 labeling strategies for sparse labeling and *in vivo* tracking of the AIB neurites
357 (Supplementary Fig. 6; Armenti et al., 2014a). It also required isotropic imaging via the
358 use of dual-view light-sheet microscopy (diSPIM) (Kumar et al., 2014; Wu et al., 2013)
359 and the development of a triple-view confocal microscope combined with a deep-
360 learning framework for enhanced resolution ((Weigert et al., 2018; Wu et al., 2016),see
361 details in Methods). Our high resolution and continuous imaging approaches in embryos
362 revealed that the stereotypic placement of the AIB neurite involves **(a)** an initial phase of
363 tip-directed outgrowth, and **(b)** relocation of part of the growing neurite to the distal
364 neighborhood by a 'zippering' mechanism, as further described below.

365 **(a) Initial tip-directed outgrowth:** We observed that the cell bodies of the bilaterally
366 symmetric AIB neurons display outgrowth of a neurite that enters the nerve ring ~ 400
367 m.p.f. The two AIB neurites then circumnavigate the nerve ring at opposite sides of the
368 neuropil—with AIBL growing dorsally on the left side of the nerve ring, and AIBR also
369 projecting dorsally, but at the right side of the ring (Fig. 5a,b). They grow along the

370 proximal neighborhood, fasciculating with the axons of amphid sensory neurons (from
371 which they later receive synaptic inputs) (Supplementary Fig. 6d). The simultaneous
372 outgrowth of the AIBL and AIBR neurons results in their neurites meeting at the dorsal
373 midline of the nerve ring at approximately 460 m.p.f. The AIB outgrowth continues past
374 their meeting point at the dorsal midline, and each AIB grows along each other, still
375 along the proximal neighborhood, at 480 m.p.f. (Fig. 5c).
376 **(b) Relocation to the distal neighborhood:** We observed that around 500 m.p.f., the
377 segment of each AIB neurite that has grown past the midline (ie, segment that will
378 constitute the future distal neurite) starts separating from its lateral counterpart (the
379 other AIB), starting from the growing tip (Fig. 5d-f, Supplementary Fig. 6e-g). The exit of
380 the tip from the proximal neighborhood takes place as it extends straight, instead of
381 following the ventral turn of the nerve ring, likely due to a loss of adhesion to proximal
382 neighborhood neurons (Supplementary Fig. 6h,i). The growing tip then encounters the
383 distal neighborhood (marked by RIM) at approximately 520 m.p.f. (Fig. 5h). Following
384 this, the entire shaft of the future distal neurite relocates to the distal neighborhood,
385 starting from the tip, and progressively 'zippering' towards the midline (Fig. 5i,j). At 510
386 minutes, 8% of the relocating distal neurite overlaps with RIM and the distal
387 neighborhood. This overlap increases to 60% at around 535 mins and 96% at around
388 560 mins, demonstrating progressive overlap over time, analogous to the fastening of a
389 zipper (see Methods). The separation or 'unzippering' from the proximal neighborhood
390 and 'zippering' onto the distal neighborhood leads to repositioning of the entire distal
391 neurite of AIB to a new neighborhood (Fig. 5j-n).

To investigate if placement of the AIB distal neurite by zippering has implications for synaptic protein distribution, we imaged presynaptic protein RAB-3 localization in the AIB distal neurite during the time when it is repositioned by zippering (520-570 m). We discovered that presynaptic proteins populate the neurite starting from the tip, progressively towards the dorsal midline in the same spatial pattern as AIB-RIM zippering-mediated contact (Supplementary Fig. 7). This suggests that the zippering mechanism might influence the spatiotemporal pattern of synaptic protein distribution in AIB upon contact with postsynaptic RIM. These findings are consistent with the observation in *syg-1(ky652)* that partial contact between AIB and RIM results in altered distribution of synaptic proteins to the sites of RIM contact.

Altogether, we discovered that the AIB neurite is positioned by a combination of tip-directed growth in the proximal neighborhood, circumferential exit of the distal neurite from the proximal neighborhood and its subsequent relocation and zippering to the distal neighborhood. The phenomenon of zippering of neurite shafts as a mechanism of fasciculation had been previously described in the context of dense primary neuron cultures (Barry et al., 2010; Šmít et al., 2017; Voyiadjis et al., 2011) but whether this occurs in developmental contexts *in vivo* is unknown. We demonstrate that the distal segment of the AIB neurite is placed in the correct neighborhood via a zippering mechanism onto a specific sublayer of the nerve ring.

414 **Increase of local expression of SYG-1 at the distal neighborhood correlates**
415 **with zippering of the distal AIB neurite onto its neighborhood**

416 To understand how SYG-1 coordinates the developmental sequence of events that
417 place the AIB neurite in specific neighborhoods, we examined the spatiotemporal
418 dynamics of expression of the *syg-1* transcriptional reporter during embryogenesis. By
419 long-term imaging using light sheet microscopy (diSPIM) we discovered that the *syg-1*
420 promoter exhibits dynamic changes in spatial expression within nerve ring sublayers
421 during the different events that occur to sequentially and precisely place the AIB neurite.

422 Similar to postembryonic animals, in embryos prior to hatching (~780 m.p.f.), the
423 *syg-1* reporter is expressed in both proximal and distal AIB neighborhoods, with
424 enrichment in the distal neighborhood (Fig. 6a-d). To investigate how this expression
425 pattern emerges during development, we imaged the dynamics of expression of the
426 *syg-1* promoter throughout the developmental period during which the AIB neurites are
427 placed in the neighborhoods (400- 570 m.p.f.) (Fig. 5a-j). We observed:

428 1. Prior to 470 m.p.f., expression of the *syg-1* reporter in the nerve ring is primarily
429 restricted to a single band corresponding to the AIB proximal neighborhood (Fig. 6e,i,i').
430 This coincides with periods of outgrowth by the AIBs in the proximal neighborhood.

431 2. Over the next two hours of embryogenesis (470-590 m.p.f.), a pair of neurons (one
432 on each side of the nerve ring) robustly expressing *syg-1* grow into, and are placed in,
433 the distal neighborhood (Fig. 6f,j,j'). Through colocalization studies we identified these
434 pair of neurons to correspond to RIMs (Supplementary Fig. 8a-c). As RIMs grow into the
435 distal neighborhood, we also observe the onset of *syg-1* expression in other distal
436 neighborhood neurons (Fig. 6f-h). Therefore, during this period (470-590 m.p.f.) *syg-1*

437 expression levels increase in the distal neighborhood due to (a) ingrowth of the *syg-1*-
438 expressing RIM neurons into the neighborhood and (b) onset of *syg-1* expression in
439 other neurons in the neighborhood. This increase in *syg-1* expression in the distal
440 neighborhood is accompanied by a progressive decrease in *syg-1* levels in the proximal
441 neighborhood (Fig. 6j-l). Mean intensities of the *syg-1* reporter in the distal
442 neighborhood relative to the proximal neighborhood increases by 2-2.4 times (between
443 470-600 m.p.f; Supplementary Fig. 8d,e).

444 These observations indicate that dynamic changes in relative levels of *syg-1*
445 between specific nerve ring neighborhoods might underlie the specific placement of the
446 single AIB neurite across these neighborhoods. Altogether we provide evidence of
447 layered expression of an IgCAM in two specific nerve ring neighborhoods, observe that
448 the expression dynamically switches between these neighborhoods and describe how
449 these dynamic changes correlate with the nanoscale precise placement of a single
450 neurite (AIB) across these neighborhoods.

451

452 **Ectopic *syg-1* expression is sufficient to alter placement of the AIB distal**
453 **neurite**

454 To investigate if *syg-1* is instructive for the placement of the AIB distal neurite in
455 the nerve ring, we ectopically increased *syg-1* levels of expression in the proximal
456 neighborhood. Through promoter screening and lineage-based cell identification, we
457 determined that during embryogenesis, promoters of the *nphp-4* and *mgl-1b* genes are
458 primarily expressed in neurons of the proximal neighborhood
459 (http://promoters.wormguides.org.) (Z. Bao et al., 2006; Boyle et al., 2006; Duncan et

460 al., 2019). Many of the neurons in which these promoters are expressed are
461 fasciculation partners of AIB in the proximal neighborhood. We used these promoters to
462 drive ectopic expression of a *syg-1* cDNA in the proximal neighborhood in the *syg-*
463 *1(ky652)* mutant background. Unlike in wild type and *syg-1* mutants (Fig. 7a-f,
464 Supplementary Fig. 9a,b), in the animals with ectopic *syg-1* expression, we observed a
465 gain-of-function phenotype in which the AIB distal neurite remains partially positioned in
466 the proximal neighborhood through postembryonic larval stages (Fig. 7g-j,
467 Supplementary Fig. 9c). Therefore ectopic expression of *syg-1* in neurons of the
468 proximal neighborhood is sufficient to misposition the AIB distal neurite segment. When
469 we ectopically expressed a *syg-1* cDNA lacking the intracellular domains, we observed
470 similar gain-of-function effects, indicating that SYG-1's extracellular Ig domains are
471 sufficient in this context (Supplementary Fig. 9d). These observations suggest that
472 SYG-1 is instructive in the placement of the AIB distal neurite into specific
473 neighborhoods, and that its spatiotemporally regulated expression in banded patterns in
474 the nerve ring is important for placement of specific neurites onto distinct neuropil
475 layers.
476

477 **SYG-1 is required for layer-specific placement of rich-club neuron AVE**

478 We next examined if *syg-1* is also important for placement of other neurites in the
479 layers in which it is highly expressed. We focused on the rich-club AVE neurons, the
480 neurites of which are also placed in two distinct neighborhoods, different from the AIB
481 neighborhoods and separated by a posterior-anterior chiasm at the dorsal midline. (Fig.
482 8a-c)(Moyle et al., 2020; Sabrin et al., 2019; Towlson et al., 2013; White et al., 1986).

483 Reconstructions from electron micrographs reveal that the AVE neurons have a
484 morphology similar to AIB, however its neurite is more anteriorly placed (by one
485 stratum) with respect to AIB (Moyle et al., 2020). Therefore the proximal neurite of AVE
486 occupies the S2/S3 neighborhood occupied by the AIB distal neurite. Since *syg-1*
487 expression is enriched in this "AIB distal/AVE proximal" neighborhood, we tested, by
488 examining AVE neurite placement relative to the RIM neurons, if placement of the AVE
489 neurite in this neighborhood is also affected in *syg-1(ky652)* mutants.

490 Although AVE and RIM are not synaptic partners, they form non-synaptic
491 contacts with each other along their neurites, as indicated by EM connectome data
492 (White et al., 1986; Witvliet et al., 2020). When we fluorescently labeled RIM and AVE in
493 wildtype animals, we observed that the proximal AVE neurite runs along the RIM
494 neurite, consistent with the EM studies (Fig. 8d,e,e'). By contrast, in *syg-1* mutants the
495 AVE proximal neurite is frequently detached from RIM (seen in 50% of *syg-1(ky652)*
496 mutants versus 9.1% in wild type (Fig. 8f,g,g',h). The dorsal midline shift of AVE is also
497 affected in *syg-1* mutant animals (mean length = 2.73 μm in *syg-1(ky652)* and 3.99 μm
498 in wild type animals; Fig. 8i). Together with the AIB studies, these observations are
499 consistent with *syg-1* expression in a S2/S3 sublayer resulting in nanoscale placement
500 of both the AIB and AVE neurites into that neighborhood.

501 In the previous sections we demonstrated that RIM has robust *syg-1* expression
502 during nerve ring development and throughout postembryonic stages. So we next
503 investigated if RIM acts as a guidepost, positioning AVE onto the S2/S3 neighborhood
504 to facilitate formation of AVE synapses onto correct partners. We observed that
505 caspase-mediated ablation of the RIM neurons results in partial defects in the

506 placement of the AVE proximal neurite (37.03% of RIM-ablated animals had defects in
507 AVE neurite placement, compared to 6.37% in wild type animals) (Fig. 8j,k). Our
508 observations suggest that layer-specific expression of *syg-1* regulates nanoscale
509 precision in placement of the AVE neurites in the AVE proximal neighborhood.
510 Together, our studies uncover spatiotemporal dynamics of expression of an adhesion
511 molecule between nerve ring neighborhoods, and its regulation of a novel zippering
512 mechanism for positioning neurites onto these specific neuropil strata.
513

514 **Discussion**

515 Nanoscale placement of rich-club interneuron AIB results in the wiring of modular
516 circuits across distinct layers of the neuropil. Neuropil layers are a conserved
517 organizational principle present in evolutionarily diverse brain regions, ranging from the
518 *C. elegans* nerve ring to the *Drosophila* lamina and the inner plexiform layer of the
519 mammalian retina (Moyle et al., 2020; Robles et al., 2011; Tan et al., 2015). Precise
520 placement of neuronal processes and their synapses, particularly for neurons spanning
521 across multiple layers, underpin brain topographic maps, and their functional and
522 structural principles (Clandinin & Feldheim, 2009). We find that in the layered nematode
523 nerve ring, "rich-club" interneuron AIB facilitates network connectivity between the
524 modular S2, S3 and S4 layers, and that its precise placement and synaptic distribution
525 in the context of the neuropil is tightly linked to its functional properties as a rich-club
526 informational hub across layers. The conserved and stereotyped design principles
527 observed for AIB, both by EM analyses and *in vivo*, are reminiscent of those seen for
528 cellular motifs in the inner plexiform layer of the vertebrate retina. For example, AII

529 amacrine cells, which distribute their neurites and synapses across distinct, but specific
530 sublaminae, receive inputs from rod bipolar axon terminals (in lower sublamina b) and
531 produce outputs onto ganglion cell dendrites (in sublamina a)(Kolb, 1995; Strettoi et al.,
532 1992). Our forward genetic screens in AIB reveal that the developmental processes
533 dictating neurite placement, and those instructing polarized distribution of pre- and
534 postsynaptic specializations across laminae, are genetically separable. Therefore in
535 AIB, the correct emergence of conserved design principles requires the modular
536 deployment of two developmental programs: polarized placement of pre- and
537 postsynaptic specializations along the neurite, and the nanoscale placement of the
538 neurite onto the correct neighborghood of the neuropil.

539 A novel zippering mechanism governs precise AIB placement onto specific
540 neighborhoods in the neuropil. The correct development of the neuropil structure
541 requires that 181 neurites, which form synapses *en passant* or along the length of their
542 axon, are precisely placed onto neighborhoods within layers. Our current mechanistic
543 frameworks of neurodevelopment are insufficient to explain how single cells make
544 simultaneous and coordinated use of similar molecular cues to achieve precise
545 placement onto specific neighborhoods within the layered neuropil. By combining light
546 sheet microscopy, a new triple-view confocal microscope and machine learning
547 approaches, we are able to resolve these developmental events for the AIB neurons of
548 *C. elegans*, and uncover an *in vivo* mechanism that places neurites onto layers via
549 zippering. Zippering has been observed and characterized in tissue culture cells, and
550 has been hypothesized to be a mechanism that could instruct neurites switching tracts
551 within bundles or fascicles (Honig et al., 1998; Šmít et al., 2017). Evidence for the *in*

552 *vivo* existence of this mechanism, or its importance in development, has been lacking.
553 We now demonstrate that zippering occurs *in vivo* in embryos, and that it is important
554 for placing neurites within specific neuropil neighborhoods during development.

555 Spatiotemporally-regulated expression of IgCAM protein SYG-1 in specific nerve
556 ring neighborhoods guide placement of AIB neurites. Our genetic studies, embryonic
557 expression studies and imaging analyses reveal that expression of this IgCAM in
558 specific nerve ring neighborhoods is dynamic, coincides with AIB developmental
559 decisions, and is necessary, non-autonomously, for AIB neurite placement onto specific
560 layers. Our findings are consistent with studies in the *Drosophila* medulla, which
561 determined that expression of DIP family of IgCAMs are restricted to specific layers or
562 layer boundaries, regulated during pupal development and probably necessary for
563 matching neuronal pairs within medullar layers (Tan et al., 2015). Moreover,
564 spatiotemporal dynamics of adhesion molecule expression encodes layer specificity in
565 the lamina of the *Drosophila* visual system, e.g., it was found that expression of the
566 adhesion molecule Cadherin-N renders neurons competent to layer-specific targeting in
567 a temporally segregated manner (Petrovic & Hummel, 2008). Our observations extend
568 these findings, now demonstrating that the spatiotemporal regulation of SYG-1 in
569 specific *C. elegans* nerve ring neighborhoods is tightly coordinated with the sequential
570 cellular decisions of AIB during the placement of its neurite segments onto specific
571 layers within the neuropil.

572 SYG-1 expression is sufficient to instruct misplacement of AIB onto ectopic
573 neighborhoods. Expression of the *syg-1* gene, first at the S3/S4 nerve ring
574 neighborhood and later at the S2/S3 neighborhood coincides with the AIB outgrowth

575 dynamics through these neighborhoods. Mis-expression of SYG-1 is sufficient to result
576 in the retention of segments of the AIB neurite onto the incorrect layer, indicative of a
577 role for SYG-1 in instructing zippering and placement of AIB onto the proper neuropil
578 layer. The Ig-CAM SYG-1 is conserved across evolution, and its orthologs (Rst and
579 Kirre in *Drosophila* and Kirrel1/2/3 in mammals) play important roles as adhesion
580 molecules in varying developmental contexts (S. Bao & Cagan, 2005; Garg et al., 2007;
581 Kim et al., 2015; Serizawa et al., 2006; Shen & Bargmann, 2003; ztokatli et al., 2012).
582 We note that while in the *C. elegans* egg-laying circuit, SYG-1 is known to interact with
583 its partner (SYG-2) to regulate synapse formation, in the context of the nerve ring, these
584 molecules appear to primarily mediate fasciculation. A loss-of-function mutant allele of
585 *syg-2* exhibits similar defects in AIB distal neurite placement (Supplementary Fig. 4d-f).
586 A loss of function mutant in *syg-2* has been previously shown to result in defasciculation
587 defects of the HSNL axon (Shen et al., 2004), and while not characterized in this study,
588 we hypothesize that similar mechanisms might underpin *syg-2* roles at the nerve ring.
589 Importantly, our findings suggest that SYG-1 role in neurite placement in nerve ring
590 neighborhoods is analogous to the role for mammalian orthologs Kirrel 2 and Kirrel3,
591 which are involved in axon sorting in the olfactory system, possibly via regulation of
592 axon fasciculation.

593 Zippering mechanisms via affinity-mediated adhesion might help instruct
594 neighborhood coherence while preserving 'fluid', or transient interactions among
595 neurites within neuropil structures. Our analyses of contact profiles for individual
596 neurons in the nerve ring neuropil reveal that most interactions between neuropil
597 neurites are brief, resulting in a 'tangled' structure with variable contact profiles across

598 connectomes (Moyle et al., 2020). Yet, neuropils, including the *C. elegans* nerve ring,
599 retain structural design features that underlie functional relationships among neurons,
600 and circuit specificity. How does the system solve this tension of flexibility and
601 stereotypicity? We speculate that dynamic expression of adhesion molecules, such as
602 SYG-1, and zippering mechanisms, might help preserve the tissue organization in the
603 tangled context of neuropils by creating affinity relationships of relative strengths. These
604 relationships could result in the separation of neuropil clusters, similar to observations in
605 developing embryos in which cell types expressing compatible cell adhesion molecules
606 were observed to phase separate onto clusters based on affinity relationships (Foty &
607 Steinberg, 2005, 2013; Steinberg, 1962). Our observations of the expression of SYG-1
608 simultaneously coordinating, not only AIB development, but also laminar placement of
609 rich club neuron AVE, suggest a layer-specific molecular signature that influences co-
610 segregation of neighboring neurites via affinity profiles. We hypothesize that in
611 neuropils, these layer-specific molecular signatures mark specific domains that enable
612 placement of neurites via flexible, differential cell-adhesion mediated zippering
613 mechanisms.
614

615 **Methods**

616

617 ***C. elegans* strains**

618 *C. elegans* strains were raised at 20°C using OP50 *Escherichia coli* seeded on
619 NGM plates. N2 Bristol is the wild-type reference strain used. We received the NC1750

620 strain from the Caenorhabditis Genetics Center (CGC). Transgenic strains used in this
621 study are available upon request.
622
623 **Molecular biology and Transgenic lines**
624 We used Gibson Assembly (New England Biolabs) or the Gateway system
625 (Invitrogen) to make plasmids used for generating transgenic *C. elegans* strains.
626 Detailed cloning information or plasmid maps will be provided upon request. Transgenic
627 strains were generated via microinjection with the construct of interest at 5-100 ng/uL by
628 standard techniques (Mello & Fire, 1995). Co-injection markers *unc-122p*: GFP or *unc-*
629 *122p*: RFP were used.
630 We generated the *syg-1* transcriptional reporter (Fig. 4a-h, Fig.6, Supplementary
631 Fig. 8) by fusing membrane-targeted PH:GFP to a 3.5 kb *syg-1* promoter region as
632 described (Schwarz et al., 2009).
633
634 **SNP mapping and Whole-Genome Sequencing**
635 We isolated mutant allele *daf-16(ola337)* and *syd-2(ola341)* from a visual forward
636 genetic screen in an integrated wild type transgenic strain (*olaIs67*) with AIB labeled
637 with cytoplasmic mCherry and AIB presynaptic sites labeled with GFP: RAB-3. Ethyl
638 methanesulfonate (EMS) mutagenesis was performed and animals were screened for
639 defects in placement of the AIB neurite, and defects in AIB presynaptic site distribution.
640 We screened F2 progeny on a Leica DM 5000 B compound microscope with an HCX
641 PL APO 63x/1.40–0.60 oil objective.

642 The novel lesions *ola337* and *ola341* were out-crossed six times to wild type (N2)
643 animals and still retained a defect in AIB distal neurite placement and AIB presynaptic
644 protein distribution, respectively. We then used single-nucleotide polymorphism (SNP)
645 mapping as described (Davis et al., 2005) to map the *ola337 and ola341* lesions.

646 We then performed whole-genome sequencing on *ola337* and *ola341* (along with
647 4 other mutants from the screen) at the Yale Center for Genome Analysis (YCGA), as
648 previously described (Sarin et al., 2008). We analyzed the results using the Galaxy
649 platform, with http://usegalaxy.org/cloudmap (Minevich et al., 2012) using the EMS
650 variant density mapping workflow. Lesion information from mutants is listed in
651 Supplementary Table 1.

652

653 **Confocal imaging of *C. elegans* larvae and image processing**

654 We used an UltraView VoX spinning disc confocal microscope with a 60x CFI
655 Plan Apo VC, NA 1.4, oil objective on a NikonTi-E stand (PerkinElmer) with a
656 Hammamatsu C9100–50 camera. We imaged the following fluorescently tagged fusion
657 proteins, eGFP, GFP, PH:GFP (membrane-tethered), RFP, mTagBFP1 and mCherry at
658 405, 488 or 561 nm excitation wavelength. We anesthetized *C. elegans* at room
659 temperature in 10mM levamisole (Sigma) under glass coverslips and mounted them on
660 glass slides for imaging.

661 We used the Volocity image acquisition software (Improvision by Perkin Elmer)
662 and processed our images using Fiji(Schindelin et al., 2012). Image processing included
663 maximum intensity projection, 3D projection, rotation, cropping, brightness/contrast, line
664 segment straightening, and pseudo coloring. All quantifications from confocal images

665 were conducted on maximal projections of the raw data. The simple neurite tracer Fiji
666 plugin and a MATLAB code were used to validate estimation of minimum perpendicular
667 distance between neurites. Pseudocoloring of AIBL and AIBR was performed in Fiji.
668 Pixels corresponding to the neurite of either AIBL/R were identified and the rest of the
669 pixels in the image were cleared. This was done for both neurons of the pair and the
670 resulting images were merged.

671

672 **Embryo labeling, imaging and image processing**

673 For labeling of neurites and subcellular structures in embryos, we used
674 membrane tethered PH:GFP. A subtractive labeling strategy was employed for AIB
675 embryo labeling (Supplementary Fig. 6a). Briefly, we generated a strain containing unc-
676 42p::ZF1::PH::GFP and lim-4p::SL2::ZIF-1, which degraded GFP in the sublateral
677 neurons, leaving GFP expression only in the AIB and/or ASH neurons. (Armenti et al.,
678 2014b). Onset of twitching was used as a reference to time developmental events.
679 Embryonic twitching is stereotyped and starts at 430 minutes post fertilization (m.p.f) for
680 our imaging conditions.

681 Embryonic imaging was performed via dual-view inverted light sheet microscopy
682 (diSPIM) (Kumar et al., 2014; Wu et al., 2013) and a combined triple-view line scanning
683 confocal/DL for denoising, as described below.

684

685 **Triple-view line-scanning confocal/DL**

686 We developed a triple-view microscope that can sequentially capture three
687 specimen views, each acquired using line-scanning confocal microscopy. Multiview

688 registration and deconvolution can be used to fuse the 3 views (Wu et al., 2013),
689 improving spatial resolution. Much of the hardware for this system is similar to the
690 previously published triple-view system (Wu et al., 2016), i.e., we used two 0.8 NA
691 water immersion objectives for the top views and a 1.2 NA water immersion lens placed
692 beneath the coverslip for the bottom view. To increase acquisition speed and reduce
693 photobleaching, we applied a deep-learning framework (Weigert et al., 2018) to predict
694 the triple-view result when only using data acquired from the bottom view. The training
695 datasets were established from 50 embryos (anesthetized with 0.3% sodium azide) in
696 the post-twitching stage, in which the ground truth data were the deconvolved triple view
697 confocal images, and the input data were the raw single view confocal images resulting
698 in improved resolution (270nm X 250 nm X 335nm).
699

700 **Cell lineaging**

701 Cell lineaging was performed using StarryNite/AceTree (Z. Bao et al., 2006;
702 Boyle et al., 2006; Murray et al., 2006). Light sheet microscopy and lineaging were
703 integrated to uncover cell identities in pre-twitching embryos (Duncan et al., 2019).
704 Lineaging information for promoters is available at http://promoters.wormguides.org.
705 Our integrated imaging and lineaging approaches enabled us to identify a promoter
706 region of *inx-19* which is expressed in the RIM neurons prior to RIM neurite outgrowth
707 (~370 m.p.f.) and in additional neurons in later embryonic stages. The *inx-19p* was one
708 of the promoters used for embryonic ablation of RIM (described in the next section).
709 In addition our integrated imaging and lineaging approach also enabled us to identify
710 two promoters with expression primarily in the AIB proximal neighborhoods (*nphp-4*p

711 and *mgl-1b*p). 4/4 neuron classes that were identified to have *nphp4*p expression, are in
712 the AIB proximal neighborhood (ADL/R,ASGL/R,ASHL/R,ASJL/R) and 2/3 neuron
713 classes that were identified to have *mgl-1b*p expression are in the AIB proximal
714 neighborhood (AIAL/R, ADFR) (http://promoters.wormguides.org).
715

716 **Caspase-mediated ablation of RIM neurons**

717 The RIM neurons were ablated using a split-caspase ablation system (Chelur &
718 Chalfie, 2007). We generated one set of transgenic strains with co-expression of the
719 p12 or p17 subunit of human Caspase-3, both expressed under *inx-19p* (termed
720 ablation strategy 1), and another set of ablation strains with co-expression of the p12
721 subunit expressed under *inx-19p* and p17 under *tdc-1p* (termed ablation strategy 2)
722 (Supplementary Fig. 5). L3 larvae from the RIM-ablated populations were imaged on the
723 spinning-disk confocal microscope (described earlier).

724

725 **Rendering of neurites and contacts in the EM datasets**

726 From available EM datasets (C. Brittin et al., 2018; Cook et al., 2019; White et
727 al., 1986; Witvliet et al., 2020) we rendered the segmentations of neuron boundaries in
728 2D using TrakEM2 in Fiji. TrakEM2 segmentations were volumetrically rendered by
729 using the 3D viewer plugin in Fiji (ImageJ2; downloaded from
730 https://imagej.net/Fiji#Downloads) and saved as object files (.obj), or by using the 3d
731 viewer in CytoSHOW (Duncan et al., 2019), an open source image analysis software.
732 CytoSHOW can be downloaded from http://www.cytoshow.org/ as described.

733 To generate 3D mappings of inter-neurite membrane contact, the entire
734 collection of 76,046 segmented neuron membrane boundaries from the JSH TEM
735 datasets (C. Brittin et al., 2018; C. A. Brittin et al., 2020; White et al., 1986) were
736 imported from TrakEM2 format into CytoSHOW as 2D cell-name-labelled and uniquely
737 color-coded regions of interest (ROIs). To test for membrane juxtaposition, we dilated
738 each individual cell-specific ROI by 9 pixels (40.5 nm) and tested for overlap
739 with neighboring undilated ROIs from the same EM slice. A collection of 289,012
740 regions of test-overlap were recorded as new ROIs, each bearing the color code of the
741 dilated test ROI and labeled with both cell-names from the pair of test-overlapped
742 ROIs. These "contact patch" ROIs were then grouped by cell-pair-name and rendered
743 via a marching cubes algorithm to yield 3D isosurfaces saved in .obj files. Each of the
744 8852 rendered .obj files represents all patches of close adjacency between a given pair
745 of neurons, color-coded and labeled by cell-pair name. Selected .obj files were co-
746 displayed in a CytoSHOW3D viewer window to produce views presented in Figures.
747

748 **Cosine similarity analysis for comparing AIB contacts across connectomes**

749 We performed cosine similarity analysis (Han et al., 2012) on AIB contacts in
750 available connectome datasets (C. Brittin et al., 2018; Cook et al., 2019; Witvliet et al.,
751 2020). For each available adjacency dataset(C. Brittin et al., 2018; Moyle et al., 2020;
752 Witvliet et al., 2020), we extracted vectors comprising of number of AIB contacts with
753 neurons common to all the datasets. We then performed cosine similarity analysis on
754 these vectors using the formula:

$$\frac{\sum_{i=1}^{n} A_i B_i}{\sqrt{\sum_{i=1}^{n} A_i^2}\sqrt{\sum_{i=1}^{n} B_i^2}}$$

where A and B are the two vectors under consideration with the symbol "i" denoting the i-th entry of each vector. The similarity values were plotted as a heat map for AIBL and AIBR using Prism. For the datasets L1_0hr, L1_5hr, L1_8hr, L2_23hr, L3_27hr, L4_JSH and Adult_N2U, the neuron-neuron contacts in the EM sections corresponding to the nerve ring were used.

Betweenness centrality analysis

We analyzed betweenness centrality for two of the available connectomes of different developmental stages (L1 and adult) (Witvliet et al., 2020). By treating individual components (mostly neurons) of a connectome as the vertices of a graph, we use the following definition of Betweenness Centrality for a vertex v,

$$BC(v) = \sum_{s,t:s\neq t\neq v} \frac{\lambda_{st}(v)}{\lambda_{st}}.$$

Here $\lambda_{st}(v)$ denotes the number of shortest paths between the vertices s and t, that include vertex v, whereas λ_{st} denotes the total number of shortest paths between the vertices s and t. We finally divide $BC(v)$ by $(N-1)(N-2)/2$ to normalize it to lie between 0 and 1. For our implementation we use the Brain Connectivity Toolbox (Rubinov & Sporns, 2010) of MATLAB2020, in particular, the function "betweenness_bin.m" in which we input the binary connection matrix corresponding to the L1 and adult connectomes (Witvliet et al., 2020). We made a Prism box plot (10 to

775 90 percentile) of betweenness centrality values of all components in each of the two
776 connectomes and highlighted the betweenness centrality values for AIBL and AIBR.

777

778 **Image representation, quantification and statistical analysis**

779 **Representation of AIB and AVE from confocal images –** Since we observed that the
780 proximal and distal neurites of AIBL and AIBR completely align and overlap
781 (Supplementary Fig. 1k-m) in confocal image stacks where the worms are oriented on
782 their side, for representation purposes we have used the upper 50% of z-slices in
783 confocal image stacks to make maximum intensity projections. This shows the proximal
784 neurite of AIBL in the context of the distal of AIBR (which has the same anterior-
785 posterior position as the distal neurite of AIBL) (Supplementary Fig. 2k-m), or vice
786 versa. We used the same procedure for AVEL and AVER.

787 **Quantification of penetrance of mutant phenotypes –** The percentage of mutant or
788 ablation animals exhibiting a normal AIB distal neurite trajectory was determined by
789 visualizing and scoring under the Leica compound microscope described. Animals in
790 which distal neurites of both AIBL or AIBR were placed at a uniform distance from the
791 proximal neurites were scored as having normal AIB distal neurite trajectory. The same
792 scoring protocol was followed for determining percentage of animals having normal AVE
793 distal neurite trajectory.

794 **Quantification of minimum perpendicular distance between neurites –** Minimum
795 perpendicular distances between neurites were measured by manually creating a
796 straight line selection (on Fiji) between the neurites (perpendicular to one of the

797 neurites) in the region where the gap between them is estimated to be the smallest. The
798 measurements were done on maximum intensity projections of raw confocal image
799 stacks where the worms are oriented on their side (z-stacks acquired along left right
800 axis of the worm, producing a lateral view of the neurons).

801 **Quantification of percent detachment between neurites –** The percent detachment
802 for defasciculated neurites (AIB and RIM or AVE and RIM) is calculated by the formula
803 % detachment = detached length (L_d) x 100 /total length (L_t) (also shown in Fig. 3m). L_d
804 is calculated by making a freehand line selection along the detached region of the RIM
805 neurite and measuring its length and L_t is calculated by making a freehand selection
806 along the RIM neurite for the entire length over which it contacts AIB or AVE, and
807 measuring the length of the selection. All the measurements were performed on
808 maximum intensity projections of confocal image stacks where the worms are oriented
809 on their side (z-stacks acquired along left right axis of the worm, producing a lateral
810 view of the neurons).

811 **Quantification of relative (distal) enrichment of *syg-1* reporter expression in**
812 **neighborhoods –** Relative (distal) enrichment of *syg-1* reporter expression is
813 calculated using the formula (also shown in Fig. 4i), Relative enrichment (*syg-1p*) =
814 mean distal neighborhood intensity (I_d)/mean proximal neighborhood intensity (I_p).
815 These measurements were done in transgenic animals co-expressing the AIB reporter
816 and the *syg-1* transcriptional reporter. For calculation of I_p a freehand line selection was
817 made (using Fiji) along the band of *syg-1* expression along the AIB proximal neurite (as
818 visualized with the AIB marker) and mean intensity along the selection is calculated.
819 Same was done for calculation of I_d except along the AIB distal neurite. The ratios of I_d

820 and I_p were plotted as relative (distal) enrichment values. These values were calculated
821 from maximum intensity projections of confocal image stacks where the worms are
822 oriented on their side (z-stacks acquired along left right axis of the worm, producing a
823 lateral view of the neurons). I_d/I_p was calculated from the side of the animal closer to the
824 objective, consistently across images to avoid differences due to depth artifacts.

825 **Quantification of the dorsal midline shift (chiasm) length of AIB and AVE –** The
826 dorsal midline shift (chiasm) lengths of AIB and AVE were calculated by making 3D
827 maximum intensity projections of confocal z-stacks and orienting the neuron pair to a
828 dorsal-ventral view. A straight line selection is made along the posterior-anterior shift of
829 each neuron and its length measured using Fiji.

830 **Quantification of distal neurite length of AIB –** The length of the distal neurite of AIB
831 was measured by drawing a freehand line along the region of the neurite past the
832 proximal neurite in maximum intensity projections of confocal image stacks where the
833 worms are oriented on their side (z-stacks acquired along left right axis of the worm,
834 producing a lateral view of the neurons).

835 **Quantification of the relative position of the AIB neurite during embryogenesis –**
836 The distances of the unzippering and zippering forks from the dorsal midline in Fig. 5l
837 and 5m are calculated from deconvolved maximum intensity projections of diSPIM
838 images where the neurons are oriented in an axial view. These distances are lengths
839 along the AIB neurite from the unzippering/zippering forks to the dorsal midline.

840 The distance of the zippering fork from the midline is subtracted from the total
841 length of the neurite at each timepoint to obtain the length of overlap between AIB and

842 RIM. The fraction of the length of AIB-RIM overlap to the total AIB neurite length
843 multipled by 100, yields a percentage overlap value at every timepoint. The reported
844 values of percent overlap are averages across the three independent embryo datasets
845 used for the Fig. 5m plot. These measurements are performed with CytoSHOW. We
846 performed the same steps as with the confocal images to pseudocolor the neurites for
847 representation.

848 **Quantification of the angle of exit of the developing AIB distal neurite and ventral**
849 **turn of nerve ring in embryos –** The angle of exit of the developing AIB distal neurite
850 is measured as the angle between straight line tangents drawn along the separating
851 distal segment of AIBL and the proximal neurite of AIBR and vice versa. These
852 measurements are performed on deconvolved maximum intensity projections of diSPIM
853 images where the neurons are oriented in an axial view. The angle of ventral turn of the
854 nerve ring is measured as the angle between straight line tangents drawn along
855 segments of the nerve ring on either side of the ventral bend of the nerve ring (see
856 Supplementary Fig. 6h,i). These measurements are performed with CytoSHOW.

857 **Imaging and representation of synaptic protein RAB-3 in AIB in embryos –** Time-
858 lapse imaging of presynaptic protein RAB-3 in AIB in embryos was performed using
859 diSPIM. To visualize the distribution of RAB-3 along the neurite we straightened the
860 distal neurite of each AIB neuron from maximum intensity projections where the AIB
861 neurons are oriented in the axial view.

862

863

Statistical analyses

Statistical analyses were conducted with PRISM 7 software. For each case, the chosen statistical test is described in the figure legend and “n” values are reported. Briefly, for continuous data, comparisons between two groups were determined by the Student’s t test. Error bars were reported as standard errors of the mean (SEM). For categorical data, groups were compared with Fisher’s exact test. The p values for significant differences are reported in the figure legend.

Acknowledgements

We thank Kang Shen, Harald Hutter and John Murray for providing strains and constructs. We thank Scott Emmons, Steve Cook, and Chris Brittin, and Mei Zhen and Daniel Witvliet for sharing their segmented EM data and adjacencies. We thank members of the Colón-Ramos lab for help, advice and insightful comments during manuscript preparation. We thank the Caenorhabditis Genetics Center (funded by NIH Office of Research Infrastructure Programs P40 OD010440) for *C. elegans* strains. We thank the Research Center for Minority Institutions program, the Marine Biological Laboratories (MBL), and the Instituto de Neurobiología de la Universidad de Puerto Rico for providing meeting and brainstorming platforms. H.S. and D.A.C-R. acknowledge the Whitman and Fellows program at MBL for providing funding and space for discussions valuable to this work. Research in the D.A.C-R., W.A.M., and Z. B. labs were supported by NIH grant No. R24-OD016474. Research in H.S. lab was further supported by the intramural research program of the National Institute of Biomedical Imaging and Bioengineering (NIBIB), NIH.

887 Research in Z.B. lab was further supported by an NIH center grant to MSKCC
888 (P30CA008748). Research in the D.A.C.-R. lab was further supported by NIH
889 R01NS076558, DP1NS111778 and by an HHMI Scholar Award.
890
891
892 **Figure Legends**
893
894 **Figure 1. Design principles of AIB neurite placement and synaptic positions**
895 **enable it to link two neighborhoods in the nerve ring**
896
897 **(a)** Schematic of an adult/larval *C. elegans* showing an AIB neuron (cyan) and its
898 proximal (orange) and distal (magenta) neighborhoods. The AIB neurite has a proximal
899 neurite segment (orange arrow), a posterior-anterior shift (black arrowhead, herein also
900 referred to as chiasm) at the dorsal midline (dashed straight line) and a distal neurite
901 segment (magenta arrow; on the other side of the worm, AIB cyan color muted in the
902 distal segment to reflect the position behind the pharynx, which is in gray). The region
903 occupied by the nerve ring neuropil is depicted in light brown. Note that this schematic
904 only shows one neuron of the AIB pair (AIBR and AIBL, for right and left, respectively,
905 see Supplementary Fig. 1e-j for both AIBs). Cell body is marked with an asterisk.
906 **(b,c)** Volumetric reconstruction of AIBR from the JSH electron microscopy connectome
907 dataset (White et al., 1986) in lateral (b) and axial (c) views. Postsynaptic (red) and
908 presynaptic (yellow) regions of the neurite, based on connectivity maps of AIBR, are
909 indicated. Note that the postsynaptic and presynaptic regions coincide with the proximal

910 and distal segment of the neurites, in (a). Arrowhead points to the chiasm (formed by
911 the posterior-anterior shift at the dorsal midline). Scale bar = 1 μm
912 **(d,e)** Representative confocal image showing lateral (d) and axial (e) view of an AIB
913 neuron with postsynaptic sites (red, labeled by GLR-1:GFP) and presynaptic sites
914 (yellow, labeled by mCh:RAB-3). Cell-specific expression of GLR-1 and RAB-3 was
915 achieved by using a bashed *inx-1* promoter (http://promoters.wormguides.org) (Altun et
916 al., 2008). Arrowhead points to the chiasm. Cell body is marked with an asterisk. Scale
917 bar = 10 μm, also applies to (e).
918 **(f,g)** Schematic of AIB (corresponding to the dashed box region in (a) and also images
919 in (b-e)), showing lateral (f) and axial (g) views of an AIB neuron (cyan) in the context of
920 the proximal (orange) and distal (magenta) neighborhoods in the nerve ring (light
921 brown). Dashed line represents the dorsal midline.
922 (**h,i**) Representative confocal image from a wild type L4 animal showing an AIB neuron
923 labeled with cytoplasmic mCherry (cyan) in lateral (h) and axial (i) views. Scale bar = 10
924 μm, also applies to (i-m).
925 **(j,k)** Representative confocal image from a wild type L4 animal showing an AIB
926 interneuron labeled with cytoplasmic mCherry (cyan); and RIM motor neuron labeled
927 with cytoplasmic GFP (magenta) in lateral (j) and axial (k) views. RIM-specific labeling
928 was achieved by a *cex-1* promoter (Piggott et al., 2011)
929 (http://promoters.wormguides.org). Note the colocalization of the AIB distal neurite with
930 the distal neighborhood marker RIM. The orange and magenta arrows indicate the
931 positions of the proximal and distal neighborhoods along the anterior-posterior axis.
932 Arrowhead indicates the chiasm.

933 **(l-m)** As (j,k), but with AIB (cyan) and AWC and ASE sensory neurons (orange). AWC
934 and ASE labeling was achieved by a *ceh-36* promoter (Lanjuin et al., 2003; Walton et
935 al., 2015) (http://promoters.wormguides.org). Note the colocalization of the AIB proximal
936 neurite with the proximal neighborhood markers AWC and ASE.
937
938 **Figure 2. Polarized distribution of synaptic proteins in the AIB neurite, and AIB**
939 **neurite neighborhood placement in the neuropil, are genetically separable**
940
941 **(a-d)** Representative confocal image (a-c) and schematic (d) of AIB expressing
942 cytoplasmic mCherry (a) and GFP:RAB-3 (b) in wild type L4 animals for simultaneous
943 visualization of neurite morphology and distribution of presynaptic sites. Merged image
944 (c). Cell body is marked with an asterisk. Scale bar = 10 μm, applies to panels (a-k).
945 **(e-l)** As (a-d) but in the genetic background of a novel *daf-16* mutant allele, *ola337* ((e-h;
946 see also Supplementary Table 1) and in *unc-33(e204)* mutants (i-l). Note GFP:RAB-3
947 polarized distribution to the distal parts of the neurite even in animals displaying severe
948 axon truncation, or displaying morphology and placement defects of the AIB neurite in
949 the context of the neuropil neighborhoods (also see Supplementary Fig. 3).
950
951 **Figure 3. SYG-1 is required for precise placement of the AIB distal neurite to the**
952 **distal, RIM-containing neighborhood**
953
954 **(a-d)** Representative confocal images of AIB (a) and RIM (b) neurons in a wild type
955 animal (L4 stage), and the merged image (c). The dashed box represents the region of

956 contact between the AIB and RIM neurites, magnified in (d). RIM is the main
957 postsynaptic partner for AIB (White et al., 1986) and co-localizes extensively with AIB
958 distal neurite (Arrow in (d) and Supplementary Fig. 1b,c). Scale bar = 10 μm in (a)
959 applies to (e-g) and (i-k). Scale bar = 1 μm in (d) applies to (h) and (l). Cell bodies are
960 marked with an asterisk.

961 **(e-h)** As (a-d) but in the *syg-1(ky652)* mutant background. Note the gap between the
962 AIB distal neurite and the RIM neurites (h), indicating loss of contact between the AIB
963 and RIM neurites due to defective placement of the AIB distal neurite in the RIM (distal)
964 neighborhood.

965 **(i-l)** As (a-d) and (e-h) but for a *syg-1(ky652)* mutant animal expressing a rescuing
966 cosmid (C54A10) containing the genomic region of wild type *syg-1.*

967 **(m)** Schematic and scatter plot of quantifications of the loss of contacts between the AIB
968 and RIM neurites. The extent of detachment of the AIB distal neurites from RIM, and
969 hence its deviation from the RIM neighborhood, was quantified using the indicated
970 formula (see also Methods). The cyan and magenta neurites in the schematic represent
971 the AIB distal neurite and the RIM neurites, respectively, as in the images. Scatter plot
972 depicts % detachment values for wild type (n=41), *syg-1(ky652)* mutant (n=39) and
973 cosmid rescue animals (n=16). Error bars indicate standard error of the mean (S.E.M.).
974 ****$p<0.0001$ by unpaired Student's t-test between WT and *syg-1(ky652)*, and between
975 *syg-1(ky652),* and *syg-1(ky652)* rescued with *syg-1* containing cosmid (C54A10)
976 (called *syg-1* rescue in graph).

977 **(n)** Schematic and scatter plot of quantification of minimum perpendicular distance
978 between the AIB proximal and distal neurites. Schematic indicates AIB (cyan) and RIM

979 (magenta) neurons in the context of the nerve ring (light brown) in WT and *syg-*
980 *1(ky652).* Double-headed arrows indicate perpendicular distance between the AIB
981 proximal and distal neurites in WT and *syg-1(ky652)*, respectively. Scatter plot depicts
982 minimum perpendicular distance values for wild type (n=19), *syg-1(ky652)* mutant
983 (n=29) and cosmid rescue animals (n=12) (see Methods). Error bars indicate standard
984 error of the mean (S.E.M.). ****$p<0.0001$ by unpaired Student's t-test between WT and
985 *syg-1(ky652)*, and between *syg-1(ky652)* and *syg-1(ky652)* rescued with *syg-1*
986 containing cosmid (C54A10) (called *syg-1* rescue in graph).
987
988 **Figure 4. The SYG-1-expressing RIM neurons regulate AIB distal neurite position**
989
990 **(a-d)** Representative confocal image of a wild type L3 animal co-expressing (a) a
991 membrane-targeted *syg-1* transcriptional reporter (see Methods) and (b) cytoplasmic
992 mCherry driven by the AIB-specific promoter (*inx-1p)*. (c) is a merge image of (a) and
993 (b). Since the *syg-1* reporter is membrane-targeted, it labels cell body outlines and
994 neurites (a,c). The dashed box or inset in (c) represents the region of contact between
995 AIB and neurites expressing the *syg-1* reporter, magnified in (d). Note that the *syg-1*
996 reporter shows two bands of expression in the nerve ring (a and c) which coincide with
997 the proximal and distal AIB neurites (b) and neighborhoods (orange and magenta
998 arrows). Note also that there is no membrane outline corresponding to the AIB cell body
999 (a, we drew a dashed siluette of the AIB cell body position as determined in (b)),
1000 consistent with the *syg-1* reporter not being expressed in AIB. Asterisk indicates cell

1001 body. Scale bar in (a) = 10 μm, also applies to (b-c) and (e-g). Scale bar in (d) = 1 μm,
1002 also applies to (h).
1003 **(e-h)** As (a-d), but with mTagBFP1 driven by RIM-specific promoter, *cex-1p*. Note the
1004 RIM neurite colocalizes with the anterior band of *syg-1* expression, coincident with the
1005 AIB distal neighborhood (magenta arrow). The white arrowhead in (e-g) and semi-
1006 transparent magenta outline in (e) indicates colocalization of the RIM cell body with the
1007 *syg-1* reporter.
1008 **(i)** Schematic (left) and scatter plot quantification (right) of the expression pattern of the
1009 *syg-1* reporter at the two AIB neighborhoods. The mean intensities of the *syg-1* reporter
1010 in the two neighborhoods were calculated, and the ratios of the mean distal
1011 neighborhood intensity (I_d) to the mean proximal neighborhood intensity (I_p) were plotted
1012 as the 'Relative enrichment', as shown in schematic and explained in Methods.
1013 **(j-o)** Confocal images showing AIB (labeled with cytoplasmic mCherry; (j,m)) and RIM
1014 (labeled with PH:GFP; (k,n)) and merged images (l,o) for wild type animals (j-l) and
1015 animals in which RIM was genetically ablated (m-o). RIM ablation was achieved using
1016 Strategy 2, explained in Supplementary Fig. 5 and below. Scale bar = 10 μm, also
1017 applies to (k-o).
1018 **(p)** Quantification of the penetrance of the AIB neurite placement defect as the
1019 percentage of animals with normal AIB distal neurite trajectory. Strategy 1 and Strategy
1020 2 refer to split caspase ablations (Chelur & Chalfie, 2007) using two different
1021 combinations of promoters expressed in RIM. In Strategy 1, expression of both caspase
1022 fragments was driven by an *inx-19* gene promoter. In Strategy 2, expression of one
1023 caspase fragment was driven by *inx-19p* and the other fragment by a *tdc-1* gene

1024 promoter ((Alkema et al., 2005); Supplementary Fig. 5 and
1025 http://promoters.wormguides.org)). *tdc-1p* drives expression of caspases in RIM later in
1026 embryonic development as compared to *inx-19p* (data not shown), resulting in later
1027 ablations of RIM, and weaker phenotype. ****p<0.0001 by Fisher's exact test between
1028 WT and RIM-ablated populations.
1029 **(q)** Quantification of the expressivity of the AIB neurite placement defect by measuring
1030 the minimum perpendicular distances between the AIB proximal and distal neurites (see
1031 Fig. 3n) in WT (n=28) and RIM-ablated populations (n=10 for strategy 1 and n=14 for
1032 strategy 2).****p<0.0001 by unpaired Student's t-test between WT and each of the RIM-
1033 ablated populations. Error bars indicate standard error of the mean (S.E.M.).
1034
1035 **Figure 5. The AIB neurite repositions onto the distal neighborhood via a zippering**
1036 **mechanism**
1037
1038 **(a)** Schematic of axial view of the AIB neuron pair - AIBL (cyan) and AIBR (yellow) in
1039 the context of the nerve ring (light brown) and the pharynx (grey), with distal and
1040 proximal neighborhood labeled (see Fig. 1).
1041 **(b-f)** Time-lapse showing initial placement of AIBL and AIBR in the proximal
1042 neighborhood and their subsequent separation from this neighborhood. Images are
1043 deconvolved diSPIM maximum intensity projections obtained from developing embryos.
1044 Neurons were individually pseudocolored to distinguish them (see Methods). The
1045 dashed boxes represent the dorsal half of the nerve ring and are magnified in **(b'-f')**.
1046 **(b''-f'')** are schematic diagrams representing the images in (b-f). Dashed vertical lines

1047 represent the dorsal midline. Note in (b,b',b''), the AIBL and AIBR neurites approaching
1048 the dorsal midline in the proximal neighborhood, see schematic in (a). In (c,c',c''), AIBL
1049 and AIBR have met at the dorsal midline and continue growing along each other, past
1050 the midline. The latter part of the neurite, past the midline, becomes the future distal
1051 neurite. (d,d',d'') shows the tip of the AIBL future distal neurite moving away from the
1052 proximal neighborhood and its counterpart, AIBR. The arrowhead indicates the point of
1053 separation of the AIBL distal neurite and the AIBR proximal neurite. (e,e',e'') shows
1054 further separation of the two neurites and by (f,f',f''), they have completely separated.
1055 The arrowheads in (e,e'e'') and (f,f'f'') also indicate the junction between the separating
1056 AIBL distal neurite and the AIBR proximal neurite. Scale bar = 10 μm for (b-f) and 2 μm
1057 for (b'-f'). All times are in m.p.f. (minutes post fertilization). A similar sequence of events
1058 is visualized at higher spatial resolution in Supplementary Fig. 6 using triple-view line
1059 scanning confocal microscopy.
1060 **(g)** Schematic of one AIB neuron (cyan) in the context of distal neighborhood marker
1061 RIM (magenta), the nerve ring (light brown) and the pharynx (grey).
1062 **(h-j)** Time-lapse showing placement of the AIB neurite (cyan) relative to the distal
1063 neighborhood marked by RIM (magenta). As in (b-f), images are deconvolved diSPIM
1064 maximum intensity projections and the neurons were pseudocolored. The dashed boxes
1065 represent the dorsal half of the nerve ring and are magnified in (h'-j'). Dashed line
1066 indicates dorsal midline (where the dorsal shift, or chiasm, in the adult is positioned,
1067 see Fig. 1). (h''-j'') are schematic diagrams representing the images in (h-j). Note in
1068 (h,h',h"), the tip of the AIB neurite encounters the growing RIM neurite (green
1069 arrowhead in (h'); black arrowhead in (h"). In (i,i',i''), the AIB distal neurite has partially

1070 aligned along the RIM neurites. The green arrowhead now indicates point of initial
1071 encounter of the two neurites (same as in (h') and the white arrowhead (in i') indicates
1072 the zippering event bringing the AIB and RIM neurons together in the distal
1073 neighborhood (as black arrowhead in i"). In (j,j',j") the two neurites have zippered up to
1074 the dorsal midline as indicated by the white arrowhead (j') and black arrowhead (j").
1075 Arrow in (i') indicates direction of zippering. Scale bar = 10 μm for (h-j) and 2 μm for (h'-
1076 j'). All times are in m.p.f. (minutes post fertilization).
1077 **(k)** Confocal micrograph of a postembryonic L4 animal in axial view showing the
1078 relationship of AIB-RIM as in (j). The same image as Fig. 1(k) was used as it allows
1079 visualization of one AIB of the pair due to mosaic array expression. Scale bar = 10 μm.
1080 The region in the dashed box represents dorsal part of the nerve ring, magnified in (k').
1081 Scale bar in (k') = 2 μm.
1082 **(l,m)** The white arrowheads in d' and i', which correspond to the points at which the
1083 neurites are separating or joining, are defined as the unzippering fork and zippering fork
1084 respectively. The distances of these points, from the dorsal midline, are quantified in (l)
1085 and (m) for different developmental stages in synchronized embryos as indicated in the
1086 timepoints on the x-axis (±5 mins). Error bars represent standard error of the mean
1087 (S.E.M.), n=5 in (l) and n=3 in (m).
1088 **(n)** Schematic highlights the three steps by which the AIB distal neurite is repositioned
1089 to a new neighborhood – (i) encounter with the new neighborhood; (ii) partial zippering
1090 and (iii) complete zippering onto the distal neighborhood (marked by RIM). The term
1091 "unzippering" is used to refer to the concomitant AIB detachment from the proximal
1092 neighborhood as it is placed to the distal neighborhood via zippering.

1093

1094 **Figure 6. Spatiotemporal regulation of *syg-1* expression during embryogenesis**

1095 **correlates with AIB placement in the distal neighborhood**

1096

1097 **(a)** Schematic of the axial view of the AIB neurons (cyan) with the proximal (orange

1098 arrows and dashed line) and distal (magenta arrow and dashed line) neighborhoods.

1099 **(b-d)** Deconvolved diSPIM image of a late stage embryo (~1 hr prior to hatching, or 780

1100 m.p.f.) showing colocalization of the *syg-1* reporter with the AIB proximal and distal

1101 neurites (and neighborhoods). This expression pattern of *syg-1* at this late embryonic

1102 stage is similar to that observed in postembryonic larvae (Fig. 4a-h). Scale bar = 10 μm,

1103 applies in (b-d).

1104 **(e-h)** Time-lapse images of *syg-1* reporter expression in earlier embryonic stages (450-

1105 630 m.p.f.). Images are deconvolved diSPIM maximum intensity projections. The

1106 dashed boxes represent the dorsal half of the nerve ring and are magnified in **(i-l)**. **(i'-l')**

1107 are schematic diagrams representing the images in (i-l). In (e,i,i') *syg-1* expression is

1108 primarily visible in a single band containing amphid neurites, and therefore coincident

1109 with the AIB proximal neighborhood. The magenta dashed line and magenta arrows

1110 point to the distal neighborhood and the orange arrow, to the proximal neighborhood.

1111 (f,j,j') show onset of weak *syg-1* expression in a second neuropil band (white arrow in

1112 (j)) and ingrowth of *syg-1*-expressing RIM neurites along this band (white arrowhead,

1113 see also Supplementary Fig. 8) onto the distal neighborhood. *syg-1* expression

1114 increases in the distal neighborhood and decreases in the proximal neighborhood as

1115 embryonic development progresses, and coincident with AIB developmental events that

1116 enable its transition from the proximal to the distal neighborhood (j-l), (Fig. 5a-j). Scale
1117 bar = 10 μm in (e-h) and 1 μm in (i-l).
1118
1119 **Figure 7. Ectopic *syg-1* expression is sufficient to redirect placement of the AIB**
1120 **distal neurite to ectopic neighborhoods**
1121
1122 **(a)** Schematic of lateral view of a wild type AIB neuron (cyan) in the context of the
1123 proximal (orange) and distal (magenta) neighborhoods, and the nerve ring (light brown).
1124 SYG-1 endogenous expression higher in the distal neighborhood represented by yellow
1125 arrowhead.
1126 **(b-c)** Confocal image of a wild type L4 animal with AIB (labeled with cytoplasmic
1127 mCherry and pseudocolored in cyan) and the proximal neighborhood neurons AWC and
1128 ASE (labeled with cytoplasmic GFP and pseudocolored in orange). The dashed box
1129 represents the region of contact between AIB and the proximal neighborhood neurons,
1130 magnified in (c). Scale bar = 10 μm in (b) (also applies to (e) and (h)) and 1 μm in (c),
1131 (also applied to (f) and (i). Cell body is marked with an asterisk.
1132 **(d-f)** As (a-c) but in the *syg-1(ky652)* lof (loss of function) mutant background. Note that
1133 the distal neurite is positioned away from the proximal neighborhood, as in wild type,
1134 although these animals display deffects in fasciculation with the distal neighborhood
1135 (see Fig. 3).
1136 **(g-i)** As (a-c) and (d-f) but with ectopic overexpression of *syg-1* cDNA in the proximal
1137 neighborhood neurons and in the *syg-1(ky652)* mutant background. In the schematic
1138 (g), expression of SYG-1 in the proximal neighborhood (achieved using *nphp-4p*, also

1139 see Supplementary Fig. 9c,d) is represented by yellow arrowhead. Note that the AIB
1140 distal neurite is now partially positioned in the proximal neighborhood in which *syg-1*
1141 cDNA was ectopically expressed (h,i).
1142 **(j)** Schematic (left) and scatter plot quantification (right) of minimum perpendicular
1143 distances (d_{min}, indicated by black double-headed arrow) between the AIB distal neurite
1144 and proximal neighborhood neurons in WT (n=11), *syg-1(ky652)* (n=12), and two *syg-*
1145 *1(ky652)* populations with WT *syg-1* cDNA overexpressed in two different sets of
1146 proximal neighborhood neurons via the use of *nphp-4p* and *mgl-1bp* (n=12 and 10
1147 respectively). The *nphp-4p* and *mgl-1bp* promoters are expressed primarily in proximal
1148 neighborhood neurons during embryogenesis (http://promoters.wormguides.org).
1149 **p<0.01 by unpaired Student's t-test between *syg-1(ky652)* and animals with ectopic
1150 proximal WT *syg-1* expression. Error bars indicate standard error of the mean (S.E.M.).
1151
1152 **Figure 8. SYG-1 dictates layer-specific placement of rich club interneuron AVE**
1153
1154 **(a,b)** Schematic of the lateral and axial views of command interneuron AVE (green) in
1155 the context of its neighborhoods: proximal (magenta) and distal (yellow), with the nerve
1156 ring (light brown) and pharynx (grey). Black arrowhead in (a) indicate a posterior-
1157 anterior chiasm. The magenta and yellow arrows indicate the positions of the AVE
1158 proximal and AVE distal neighborhoods, respectively. Note that while the design
1159 principles of AVE are similar to those of rich-club interneuron AIB, their positions in the
1160 nerve ring, and the strata they connect, are different (see (c), compare to
1161 Supplementary Fig. 1a for AIB).

1162 **(c)** Volumetric reconstruction of the AVE neuron (green) in the context of the nerve ring
1163 strata S2 (purple) and S3 (orange). Note the placement of the AVE proximal neurite
1164 along the border of S2 and S3, and the AVE distal neurite at the anterior boundary of S2
1165 (the anterior boundary abuts S1, not shown here). The dashed lines indicate the layer
1166 borders. Scale bar = 1 μm.
1167 **(d)** Confocal image of an L4 animal with AVE and RIM co-labeled. The magenta and
1168 yellow arrows indicate the positions of the AVE proximal and AVE distal neighborhoods,
1169 respectively. White arrowhead indicates AVE chiasm, corresponding to its anterior shift.
1170 Dashed box shows region of contact of the AVE and RIM neurites, magnified in **(e). (e')**
1171 is a schematic of the image in (e). Note the region of contact between the AVE proximal
1172 neurite and the RIM neurites (e,e'), in the context of AVE, in the AVE proximal
1173 neighborhood (as compared to RIM position in AIB distal neighborhood). Scale bar
1174 corresponds to 10 μm in (d) and 1 μm in (e). Scale bars in (d) and (e) apply to (f) and
1175 (g) respectively. Cell bodies are marked with an asterisk.
1176 **(f,g,g')** As (d,e,e') but in *syg-1(ky652)* mutant background. Note the gap between the
1177 AVE proximal neurite and the RIM neurites (f,g,g') and defect in the dorsal midline shift.
1178 **(h)** Scatter plot showing quantification of the loss of contacts between the AVE and RIM
1179 neurites. The extent of detachment of the AVE proximal neurites from RIM, and hence
1180 its deviation from the RIM neighborhood, was quantified using the indicated formula in
1181 Fig. 3m (also see Methods). Scatter plot depicts % detachment values for wild type
1182 (n=22) and *syg-1(ky652)* (n=16). Error bars indicate standard error of the mean
1183 (S.E.M.). **$p<0.01$ by unpaired Student's t-test between WT and *syg-1(ky652)*.

1184 **(i)** Quantification of length of the posterior-anterior shift, quantified for each AVE neurite,
1185 for WT(n=32) and *syg-1(ky652)* mutants (n=40) and displayed as a scatter plot. Error
1186 bars indicate standard error of the mean (S.E.M.). ***p<0.001 by unpaired Student's t-
1187 test between WT and *syg-1(ky652)*.
1188 **(j)** Confocal image of an AVE neuron in L3 animals with RIM neurons ablated using
1189 ablation strategy 2 (Supplementary Fig. 5 and Methods). Note altered placement of the
1190 AVE proximal neurite with respect to the proximal neighborhood (indicated by the
1191 magenta dashed line and the magenta arrow). Scale bar = 10 μm.
1192 **(k)** The percentage of animals having altered AVE distal neurite trajectory are plotted for
1193 WT (n=31) and RIM ablated populations (n=27). *p<0.1 by Fisher's exact test between
1194 WT and the RIM-ablated population.
1195
1196
1197 **References**
1198
1199 Alkema, M. J., Hunter-Ensor, M., Ringstad, N., & Horvitz, H. R. (2005). Tyramine
1200 functions independently of octopamine in the Caenorhabditis elegans
1201 nervous system. *Neuron*. https://doi.org/10.1016/j.neuron.2005.02.024
1202 Altun, Z. F., Chen, B., Wang, Z. W., & Hall, D. H. (2008). High resolution map of
1203 Caenorhabditis elegans gap junction proteins. *Developmental Dynamics*.
1204 https://doi.org/10.1002/dvdy.22025
1205 Armenti, S. T., Lohmer, L. L., Sherwood, D. R., & Nance, J. (2014a).
1206 Repurposing an endogenous degradation system for rapid and targeted
1207 depletion of C. elegans proteins. *Development (Cambridge)*.
1208 https://doi.org/10.1242/dev.115048

Armenti, S. T., Lohmer, L. L., Sherwood, D. R., & Nance, J. (2014b). Repurposing an endogenous degradation system for rapid and targeted depletion of C. elegans proteins. *Development (Cambridge)*. https://doi.org/10.1242/dev.115048

Bao, S., & Cagan, R. (2005). Preferential Adhesion Mediated by Hibris and Roughest Regulates Morphogenesis and Patterning in the Drosophila Eye. *Developmental Cell*, *8*(6), 925–935. https://doi.org/https://doi.org/10.1016/j.devcel.2005.03.011

Bao, Z., Murray, J. I., Boyle, T., Ooi, S. L., Sandel, M. J., & Waterston, R. H. (2006). Automated cell lineage tracing in Caenorhabditis elegans. *Proceedings of the National Academy of Sciences of the United States of America*. https://doi.org/10.1073/pnas.0511111103

Barry, J., Gu, Y., & Gu, C. (2010). Polarized targeting of L1-CAM regulates axonal and dendritic bundling in vitro. *European Journal of Neuroscience*. https://doi.org/10.1111/j.1460-9568.2010.07447.x

Barstead, R., Moulder, G., Cobb, B., Frazee, S., Henthorn, D., Holmes, J., Jerebie, D., Landsdale, M., Osborn, J., Pritchett, C., Robertson, J., Rummage, J., Stokes, E., Vishwanathan, M., Mitani, S., Gengyo-Ando, K., Funatsu, O., Hori, S., Imae, R., … Zapf, R. (2012). Large-scale screening for targeted knockouts in the caenorhabditis elegans genome. *G3: Genes, Genomes, Genetics*. https://doi.org/10.1534/g3.112.003830

Boyle, T. J., Bao, Z., Murray, J. I., Araya, C. L., & Waterston, R. H. (2006). AceTree: A tool for visual analysis of Caenorhabditis elegans embryogenesis. *BMC Bioinformatics*. https://doi.org/10.1186/1471-2105-7-275

Brittin, C. A., Cook, S. J., Hall, D. H., & Emmons, S. W. (2020). Beyond the connectome : A map of a brain architecture derived from whole-brain volumetric reconstructions. *BioRxiv*.

Brittin, C., Cook, S., Hall, D., Emmons, S., & Cohen, N. (2018). Volumetric

reconstruction of main Caenorhabditis elegans neuropil at two different time points. *BioRxiv*. https://doi.org/10.1101/485771

Chalasani, S. H., Chronis, N., Tsunozaki, M., Gray, J. M., Ramot, D., Goodman, M. B., & Bargmann, C. I. (2007). Dissecting a circuit for olfactory behaviour in Caenorhabditis elegans. *Nature*. https://doi.org/10.1038/nature06292

Chelur, D. S., & Chalfie, M. (2007). Targeted cell killing by reconstituted caspases. *Proceedings of the National Academy of Sciences of the United States of America*. https://doi.org/10.1073/pnas.0610877104

Christensen, R., de la Torre-Ubieta, L., Bonni, A., & Colón-Ramos, D. A. (2011). A conserved PTEN/FOXO pathway regulates neuronal morphology during C. elegans development. *Development*, *138*(23), 5257 LP – 5267. https://doi.org/10.1242/dev.069062

Clandinin, T. R., & Feldheim, D. A. (2009). Making a visual map: mechanisms and molecules. In *Current Opinion in Neurobiology*. https://doi.org/10.1016/j.conb.2009.04.011

Cook, S. J., Jarrell, T. A., Brittin, C. A., Wang, Y., Bloniarz, A. E., Yakovlev, M. A., Nguyen, K. C. Q., Tang, L. T. H., Bayer, E. A., Duerr, J. S., Bülow, H. E., Hobert, O., Hall, D. H., & Emmons, S. W. (2019). Whole-animal connectomes of both Caenorhabditis elegans sexes. *Nature*. https://doi.org/10.1038/s41586-019-1352-7

Davis, M. W., Hammarlund, M., Harrach, T., Hullett, P., Olsen, S., & Jorgensen, E. M. (2005). Rapid single nucleotide polymophism mapping in C. elegans. *BMC Genomics*. https://doi.org/10.1186/1471-2164-6-118

Demb, J. B., & Singer, J. H. (2012). Intrinsic properties and functional circuitry of the AII amacrine cell. In *Visual Neuroscience*. https://doi.org/10.1017/S0952523811000368

Duncan, L. H., Moyle, M. W., Shao, L., Sengupta, T., Ikegami, R., Kumar, A., Guo, M., Christensen, R., Santella, A., Bao, Z., Shroff, H., Mohler, W., & Colón-Ramos, D. A. (2019). Isotropic light-sheet microscopy and automated

cell lineage analyses to catalogue caenorhabditis elegans embryogenesis with subcellular resolution. *Journal of Visualized Experiments*. https://doi.org/10.3791/59533

Fan, J., Ji, T., Wang, K., Huang, J., Wang, M., Manning, L., Dong, X., Shi, Y., Zhang, X., Shao, Z., & Colón-Ramos, D. A. (2020). A muscle-epidermis-glia signaling axis sustains synaptic specificity during allometric growth in caenorhabditis elegans. *ELife*. https://doi.org/10.7554/eLife.55890

Foty, R. A., & Steinberg, M. S. (2005). The differential adhesion hypothesis: A direct evaluation. *Developmental Biology*. https://doi.org/10.1016/j.ydbio.2004.11.012

Foty, R. A., & Steinberg, M. S. (2013). Differential adhesion in model systems. In *Wiley interdisciplinary reviews. Developmental biology*. https://doi.org/10.1002/wdev.104

Gabriel, J. P., Trivedi, C. A., Maurer, C. M., Ryu, S., & Bollmann, J. H. (2012). Layer-Specific Targeting of Direction-Selective Neurons in the Zebrafish Optic Tectum. *Neuron*, *76*(6), 1147–1160. https://doi.org/https://doi.org/10.1016/j.neuron.2012.12.003

Garg, P., Verma, R., Nihalani, D., Johnstone, D. B., & Holzman, L. B. (2007). Neph1 Cooperates with Nephrin To Transduce a Signal That Induces Actin Polymerization. *Molecular and Cellular Biology*. https://doi.org/10.1128/mcb.00948-07

Gray, J. M., Hill, J. J., & Bargmann, C. I. (2005). A circuit for navigation in Caenorhabditis elegans. *Proceedings of the National Academy of Sciences of the United States of America*. https://doi.org/10.1073/pnas.0409009101

Grossman, E. N., Giurumescu, C. A., & Chisholm, A. D. (2013). Mechanisms of ephrin receptor protein kinase-independent signaling in amphid axon guidance in Caenorhabditis elegans. *Genetics*. https://doi.org/10.1534/genetics.113.154393

Han, J., Kamber, M., & Pei, J. (2012). Data Mining: Concepts and Techniques. In

Data Mining: Concepts and Techniques. https://doi.org/10.1016/C2009-0-61819-5

Hong, R. L., Riebesell, M., Bumbarger, D. J., Cook, S. J., Carstensen, H. R., Sarpolaki, T., Cochella, L., Castrejon, J., Moreno, E., Sieriebriennikov, B., Hobert, O., & Sommer, R. J. (2019). Evolution of neuronal anatomy and circuitry in two highly divergent nematode species. *ELife*. https://doi.org/10.7554/eLife.47155

Honig, M. G., Frase, P. A., & Camilli, S. J. (1998). The spatial relationships among cutaneous, muscle sensory and motoneuron axone during development of the chick hindlimb. *Development*.

Kang, C., & Avery, L. (2009). Systemic regulation of starvation response in Caenorhabditis elegans. *Genes and Development*. https://doi.org/10.1101/gad.1723409

Kim, J. H., Ren, Y., Ng, W. P., Li, S., Son, S., Kee, Y. S., Zhang, S., Zhang, G., Fletcher, D. A., Robinson, D. N., & Chen, E. H. (2015). Mechanical Tension Drives Cell Membrane Fusion. *Developmental Cell*. https://doi.org/10.1016/j.devcel.2015.01.005

Kolb, H. (1995). Roles of Amacrine Cells. In *Webvision: The Organization of the Retina and Visual System*.

Kolodkin, A. L., & Hiesinger, P. R. (2017). Wiring visual systems: common and divergent mechanisms and principles. In *Current Opinion in Neurobiology*. https://doi.org/10.1016/j.conb.2016.12.006

Kumar, A., Wu, Y., Christensen, R., Chandris, P., Gandler, W., McCreedy, E., Bokinsky, A., Colón-Ramos, D. A., Bao, Z., McAuliffe, M., Rondeau, G., & Shroff, H. (2014). Dual-view plane illumination microscopy for rapid and spatially isotropic imaging. *Nature Protocols*. https://doi.org/10.1038/nprot.2014.172

Kunzevitzky, N. J., Willeford, K. T., Feuer, W. J., Almeida, M. V., & Goldberg, J. L. (2013). Amacrine cell subtypes differ in their intrinsic neurite growth

capacity. *Investigative Ophthalmology and Visual Science*. https://doi.org/10.1167/iovs.13-12691

Lanjuin, A., VanHoven, M. K., Bargmann, C. I., Thompson, J. K., & Sengupta, P. (2003). Otx/otd homeobox genes specify distinct sensory neuron identities in C. elegans. *Developmental Cell*. https://doi.org/10.1016/S1534-5807(03)00293-4

Marc, R. E., Anderson, J. R., Jones, B. W., Sigulinsky, C. L., & Lauritzen, J. S. (2014). The All amacrine cell connectome: A dense network hub. *Frontiers in Neural Circuits*. https://doi.org/10.3389/fncir.2014.00104

Maynard, D. M. (1962). Organization of Neuropil. *Am. Zoologist*, *2*, 79–96.

Mello, C., & Fire, A. (1995). DNA Transformation. *Methods in Cell Biology*. https://doi.org/10.1016/S0091-679X(08)61399-0

Millard, S. S., & Pecot, M. Y. (2018). Strategies for assembling columns and layers in the Drosophila visual system. In *Neural Development*. https://doi.org/10.1186/s13064-018-0106-9

Minevich, G., Park, D. S., Blankenberg, D., Poole, R. J., & Hobert, O. (2012). CloudMap: A cloud-based pipeline for analysis of mutant genome sequences. *Genetics*. https://doi.org/10.1534/genetics.112.144204

Moyle, M. W., Barnes, K. M., Kuchroo, M., Gonopolskiy, A., Duncan, L. H., Sengupta, T., Shao, L., Guo, M., Santella, A., Christensen, R., Kumar, A., Wu, Y., Moon, K. R., Wolf, G., Krishnaswamy, S., Bao, Z., Shroff, H., Mohler, W., & Colón-Ramos, D. A. (2020). Structural and developmental principles of neuropil assembly in C. elegans *BioRxiv*, 2020.03.15.992222. https://doi.org/10.1101/2020.03.15.992222

Murray, J. I., Bao, Z., Boyle, T. J., & Waterston, R. H. (2006). The lineaging of fluorescently-labeled Caenorhabditis elegans embryos with StarryNite and AceTree. *Nature Protocols*. https://doi.org/10.1038/nprot.2006.222

Nevin, L. M., Taylor, M. R., & Baier, H. (2008). Hardwiring of fine synaptic layers in the zebrafish visual pathway. *Neural Development*.

https://doi.org/10.1186/1749-8104-3-36

Petrovic, M., & Hummel, T. (2008a). Temporal identity in axonal target layer recognition. *Nature*. https://doi.org/10.1038/nature07407

Petrovic, M., & Hummel, T. (2008b). Temporal identity in axonal target layer recognition. *Nature*. https://doi.org/10.1038/nature07407

Piggott, B. J., Liu, J., Feng, Z., Wescott, S. A., & Xu, X. Z. S. (2011). The neural circuits and synaptic mechanisms underlying motor initiation in C. elegans. *Cell*. https://doi.org/10.1016/j.cell.2011.08.053

Poskanzer, K., Needleman, L. A., Bozdagi, O., & Huntley, G. W. (2003). N-cadherin regulates ingrowth and laminar targeting of thalamocortical axons. *The Journal of Neuroscience : The Official Journal of the Society for Neuroscience*.

Robles, E., Filosa, A., & Baier, H. (2013). Precise lamination of retinal axons generates multiple parallel input pathways in the tectum. *Journal of Neuroscience*. https://doi.org/10.1523/JNEUROSCI.4990-12.2013

Robles, E., Smith, S. J., & Baier, H. (2011). Characterization of genetically targeted neuron types in the zebrafish optic tectum. *Frontiers in Neural Circuits*. https://doi.org/10.3389/fncir.2011.00001

Rubinov, M., & Sporns, O. (2010). Complex network measures of brain connectivity: Uses and interpretations. *NeuroImage*. https://doi.org/10.1016/j.neuroimage.2009.10.003

Sabrin, K., Wei, Y., van den Heuvel, M., & Dovrolis, C. (2019). The hourglass organization of the Caenorhabditis elegans connectome. *BioRxiv*. https://doi.org/10.1101/600999

Sanes, J. R., & Zipursky, S. L. (2010). Design Principles of Insect and Vertebrate Visual Systems. In *Neuron*. https://doi.org/10.1016/j.neuron.2010.01.018

Sanes, J. R., & Zipursky, S. L. (2020). Synaptic Specificity, Recognition Molecules, and Assembly of Neural Circuits. In *Cell*. https://doi.org/10.1016/j.cell.2020.04.008

Santella, A., Du, Z., & Bao, Z. (2014). A semi-local neighborhood-based framework for probabilistic cell lineage tracing. *BMC Bioinformatics*. https://doi.org/10.1186/1471-2105-15-217

Sarin, S., Prabhu, S., O'Meara, M. M., Pe'er, I., & Hobert, O. (2008). Caenorhabditis elegans mutant allele identification by whole-genome sequencing. *Nature Methods*. https://doi.org/10.1038/nmeth.1249

Schindelin, J., Arganda-Carreras, I., Frise, E., Kaynig, V., Longair, M., Pietzsch, T., Preibisch, S., Rueden, C., Saalfeld, S., Schmid, B., Tinevez, J. Y., White, D. J., Hartenstein, V., Eliceiri, K., Tomancak, P., & Cardona, A. (2012). Fiji: An open-source platform for biological-image analysis. In *Nature Methods*. https://doi.org/10.1038/nmeth.2019

Schürmann, F. W. (2016). Fine structure of synaptic sites and circuits in mushroom bodies of insect brains. In *Arthropod Structure and Development*. https://doi.org/10.1016/j.asd.2016.08.005

Schwabe, T., Borycz, J. A., Meinertzhagen, I. A., & Clandinin, T. R. (2014). Differential adhesion determines the organization of synaptic fascicles in the drosophila visual system. *Current Biology*. https://doi.org/10.1016/j.cub.2014.04.047

Schwarz, V., Pan, J., Voltmer-Irsch, S., & Hutter, H. (2009). IgCAMs redundantly control axon navigation in Caenorhabditis elegans. *Neural Development*. https://doi.org/10.1186/1749-8104-4-13

Serizawa, S., Miyamichi, K., Takeuchi, H., Yamagishi, Y., Suzuki, M., & Sakano, H. (2006). A Neuronal Identity Code for the Odorant Receptor-Specific and Activity-Dependent Axon Sorting. *Cell*. https://doi.org/10.1016/j.cell.2006.10.031

Shen, K., & Bargmann, C. I. (2003). The immunoglobulin superfamily protein SYG-1 determines the location of specific synapses in C. elegans. *Cell*. https://doi.org/10.1016/S0092-8674(03)00113-2

Shen, K., Fetter, R. D., & Bargmann, C. I. (2004). Synaptic specificity is

generated by the synaptic guidepost protein SYG-2 and its receptor, SYG-1. *Cell*. https://doi.org/10.1016/S0092-8674(04)00251-X

Šmít, D., Fouquet, C., Pincet, F., Zapotocky, M., & Trembleau, A. (2017). Axon tension regulates fasciculation/defasciculation through the control of axon shaft zippering. *ELife*. https://doi.org/10.7554/eLife.19907

Soiza-Reilly, M., & Commons, K. G. (2014). Unraveling the architecture of the dorsal raphe synaptic neuropil using high-resolution neuroanatomy. In *Frontiers in Neural Circuits*. https://doi.org/10.3389/fncir.2014.00105

Steinberg, M. S. (1962). Mechanism of tissue reconstruction by dissociated cells, II: Time-course of events. *Science*. https://doi.org/10.1126/science.137.3532.762

Strettoi, E., Raviola, E., & Dacheux, R. F. (1992). Synaptic connections of the narrow-field, bistratified rod amacrine cell (AII) in the rabbit retina. *Journal of Comparative Neurology*. https://doi.org/10.1002/cne.903250203

Tan, L., Zhang, K. X., Pecot, M. Y., Nagarkar-Jaiswal, S., Lee, P. T., Takemura, S. Y., McEwen, J. M., Nern, A., Xu, S., Tadros, W., Chen, Z., Zinn, K., Bellen, H. J., Morey, M., & Zipursky, S. L. (2015). Ig Superfamily Ligand and Receptor Pairs Expressed in Synaptic Partners in Drosophila. *Cell*. https://doi.org/10.1016/j.cell.2015.11.021

Taylor, W. R., & Smith, R. G. (2012). The role of starburst amacrine cells in visual signal processing. *Visual Neuroscience*. https://doi.org/10.1017/S0952523811000393

Towlson, E. K., Vértes, P. E., Ahnert, S. E., Schafer, W. R., & Bullmore, E. T. (2013). The rich club of the C. elegans neuronal connectome. *Journal of Neuroscience*. https://doi.org/10.1523/JNEUROSCI.3784-12.2013

Voyiadjis, A. G., Doumi, M., Curcio, E., & Shinbrot, T. (2011). Fasciculation and defasciculation of neurite bundles on micropatterned substrates. *Annals of Biomedical Engineering*. https://doi.org/10.1007/s10439-010-0168-2

Wakabayashi, T., Kitagawa, I., & Shingai, R. (2004). Neurons regulating the

duration of forward locomotion in Caenorhabditis elegans. *Neuroscience Research*. https://doi.org/10.1016/j.neures.2004.06.005

Walton, T., Preston, E., Nair, G., Zacharias, A. L., Raj, A., & Murray, J. I. (2015). The Bicoid Class Homeodomain Factors ceh-36/OTX and unc-30/PITX Cooperate in C. elegans Embryonic Progenitor Cells to Regulate Robust Development. *PLoS Genetics*. https://doi.org/10.1371/journal.pgen.1005003

Ware, R. W., Clark, D., Crossland, K., & Russell, R. L. (1975). The nerve ring of the nematode Caenorhabditis elegans: Sensory input and motor output. *Journal of Comparative Neurology*. https://doi.org/10.1002/cne.901620106

Weigert, M., Schmidt, U., Boothe, T., Müller, A., Dibrov, A., Jain, A., Wilhelm, B., Schmidt, D., Broaddus, C., Culley, S., Rocha-Martins, M., Segovia-Miranda, F., Norden, C., Henriques, R., Zerial, M., Solimena, M., Rink, J., Tomancak, P., Royer, L., … Myers, E. W. (2018). Content-aware image restoration: pushing the limits of fluorescence microscopy. *Nature Methods*. https://doi.org/10.1038/s41592-018-0216-7

White, J. G., Southgate, E., Thomson, J. N., & Brenner, S. (1983). Factors that determine connectivity in the nervous system of Caenorhabditis elegans. *Cold Spring Harbor Symposia on Quantitative Biology*. https://doi.org/10.1101/sqb.1983.048.01.067

White, J. G., Southgate, E., Thomson, J. N., & Brenner, S. (1986). The structure of the nervous system of the nematode C. elegans. *Philosophical Transactions of the Royal Society of London - Series B: Biological Sciences*.

Witvliet, D., Mulcahy, B., Mitchell, J. K., Meirovitch, Y., Berger, D. R., Wu, Y., Liu, Y., Koh, W. X., Parvathala, R., Holmyard, D., Schalek, R. L., Shavit, N., Chisholm, A. D., Lichtman, J. W., Samuel, A. D. T., & Zhen, M. (2020). Connectomes across development reveal principles of brain maturation in C. elegans *BioRxiv*, 2020.04.30.066209. https://doi.org/10.1101/2020.04.30.066209

Wu, Y., Chandris, P., Winter, P. W., Kim, E. Y., Jaumouillé, V., Kumar, A., Guo,

M., Leung, J. M., Smith, C., Rey-Suarez, I., Liu, H., Waterman, C. M., Ramamurthi, K. S., La Riviere, P. J., & Shroff, H. (2016). Simultaneous multiview capture and fusion improves spatial resolution in wide-field and light-sheet microscopy. *Optica*. https://doi.org/10.1364/optica.3.000897

Wu, Y., Wawrzusin, P., Senseney, J., Fischer, R. S., Christensen, R., Santella, A., York, A. G., Winter, P. W., Waterman, C. M., Bao, Z., Colón-Ramos, D. A., McAuliffe, M., & Shroff, H. (2013). Spatially isotropic four-dimensional imaging with dual-view plane illumination microscopy. *Nature Biotechnology*. https://doi.org/10.1038/nbt.2713

Xu, C. S., Januszewski, M., Lu, Z., Takemura, S., Hayworth, K. J., Huang, G., Shinomiya, K., Maitin-Shepard, J., Ackerman, D., Berg, S., Blakely, T., Bogovic, J., Clements, J., Dolafi, T., Hubbard, P., Kainmueller, D., Katz, W., Kawase, T., Khairy, K. A., … Plaza, S. M. (2020). A Connectome of the Adult Drosophila Central Brain. *BioRxiv*, 2020.01.21.911859. https://doi.org/10.1101/2020.01.21.911859

Xuan, Z., Manning, L., Nelson, J., Richmond, J. E., Colón-Ramos, D. A., Shen, K., & Kurshan, P. T. (2017). Clarinet (CLA-1), a novel active zone protein required for synaptic vesicle clustering and release. *ELife*. https://doi.org/10.7554/eLife.29276

Yamagata, M., & Sanes, J. R. (2008). Dscam and Sidekick proteins direct lamina-specific synaptic connections in vertebrate retina. *Nature*. https://doi.org/10.1038/nature06469

Yamagata, M., & Sanes, J. R. (2012). Expanding the Ig superfamily code for laminar specificity in retina: Expression and role of contactins. *Journal of Neuroscience*. https://doi.org/10.1523/JNEUROSCI.3193-12.2012

Yoshimura, S., Murray, J. I., Lu, Y., Waterston, R. H., & Shaham, S. (2008). mls-2 and vab-3 control glia development, hlh-17/Olig expression and glia-dependent neurite extension in C. elegans

Development, *135*(13), 2263 LP – 2275. https://doi.org/10.1242/dev.019547

Zallen, J. A., Kirch, S. A., & Bargmann, C. I. (1999). Genes required for axon pathfinding and extension in the C. elegans nerve ring. *Development*.

Zhen, M., & Jin, Y. (1999). The liprin protein SYD-2 regulates the differentiation of presynaptic termini in C. elegans. *Nature*. https://doi.org/10.1038/43886

Zheng, Z., Lauritzen, J. S., Perlman, E., Robinson, C. G., Nichols, M., Milkie, D., Torrens, O., Price, J., Fisher, C. B., Sharifi, N., Calle-Schuler, S. A., Kmecova, L., Ali, I. J., Karsh, B., Trautman, E. T., Bogovic, J. A., Hanslovsky, P., Jefferis, G. S. X. E., Kazhdan, M., … Bock, D. D. (2018). A Complete Electron Microscopy Volume of the Brain of Adult Drosophila melanogaster. *Cell*, *174*(3), 730-743.e22. https://doi.org/10.1016/j.cell.2018.06.019

ztokatli, H. Ö., Hörnberg, M., Berghard, A., & Bohm, S. (2012). Retinoic acid receptor and CNGA2 channel signaling are part of a regulatory feedback loop controlling axonal convergence and survival of olfactory sensory neurons. *The FASEB Journal*. https://doi.org/10.1096/fj.11-192450

Figure 1

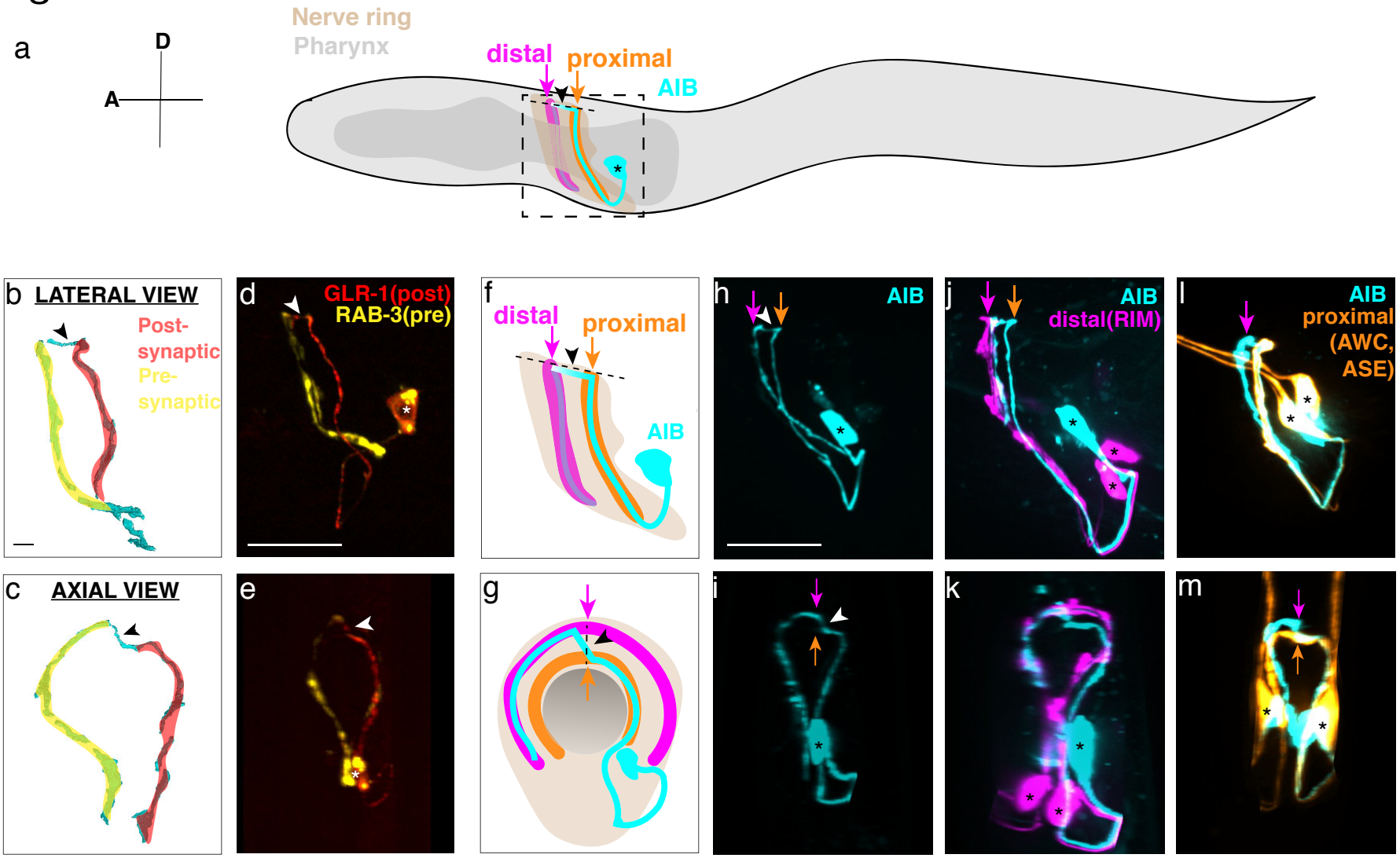
a
D
A
Nerve ring
Pharynx
distal
proximal
AIB
b LATERAL VIEW
Post-synaptic
Pre-synaptic
c AXIAL VIEW
d
GLR-1(post)
RAB-3(pre)
e
f
distal
proximal
AIB
g
h
AIB
i
j
AIB
distal(RIM)
k
l
AIB
proximal
(AWC,
ASE)
m

Figure 2

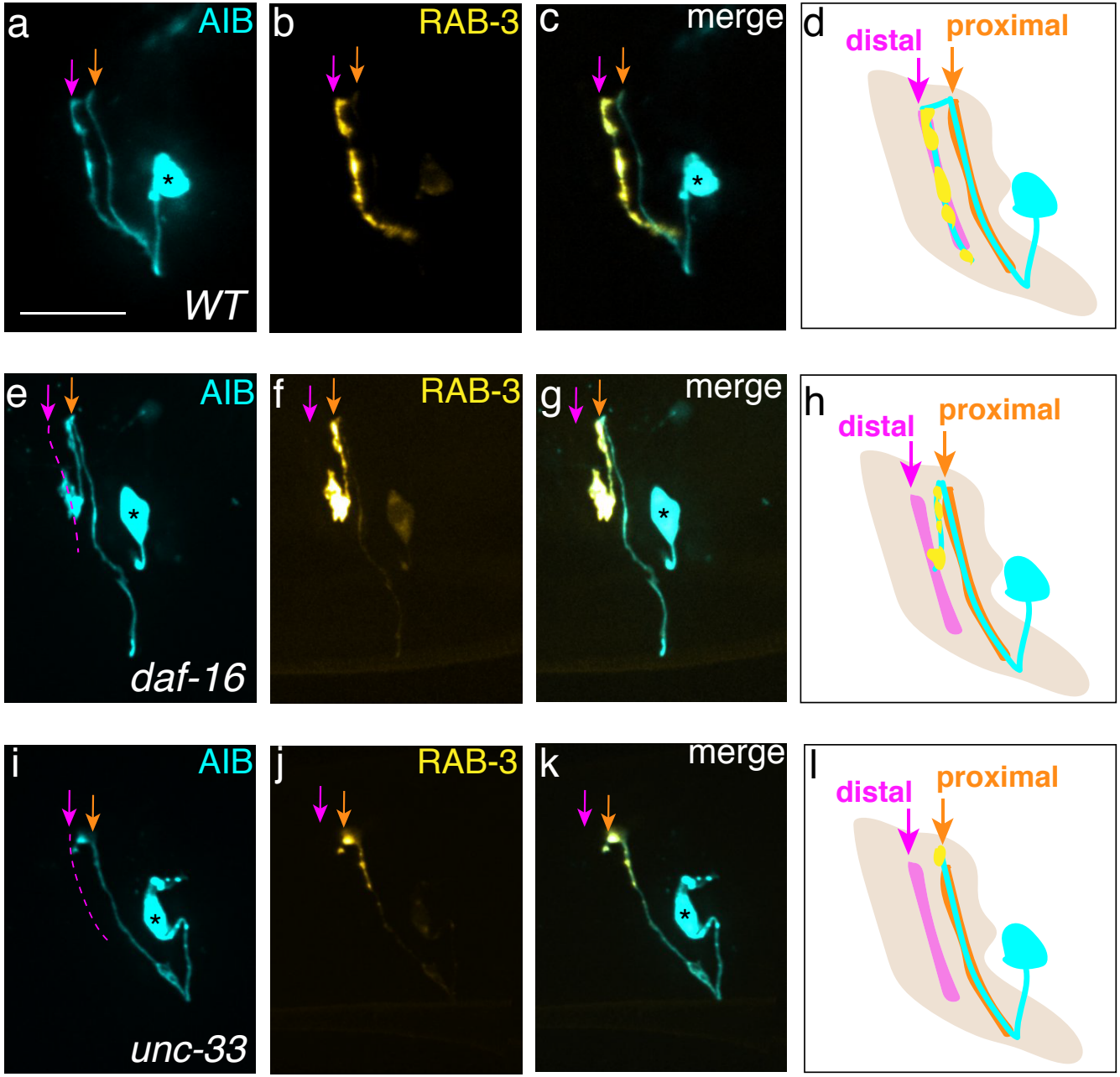
a
AIB
WT
b
RAB-3
c
merge
d
distal
proximal
e
AIB
daf-16
f
RAB-3
g
merge
h
distal
proximal
i
AIB
unc-33
j
RAB-3
k
merge
l
distal
proximal

Figure 3

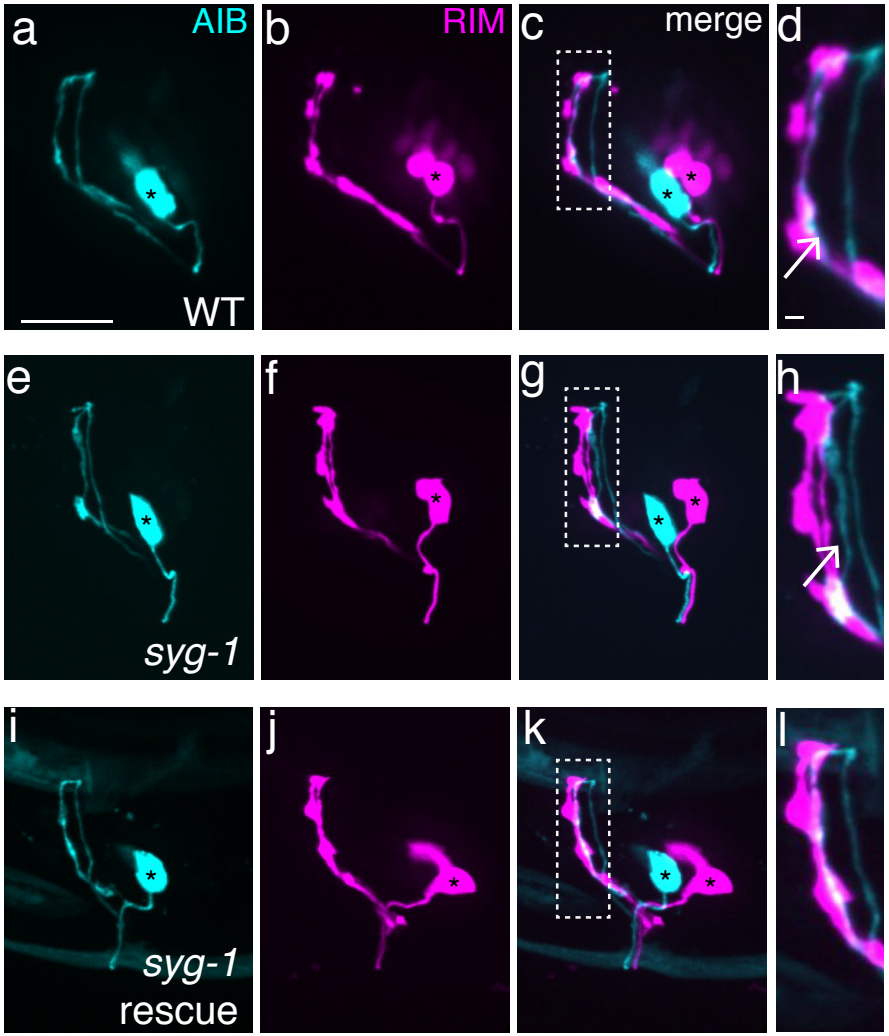
a
AIB
WT
b
RIM
c
merge
d
e
syg-1
f
g
h
i
syg-1
rescue
j
k
l

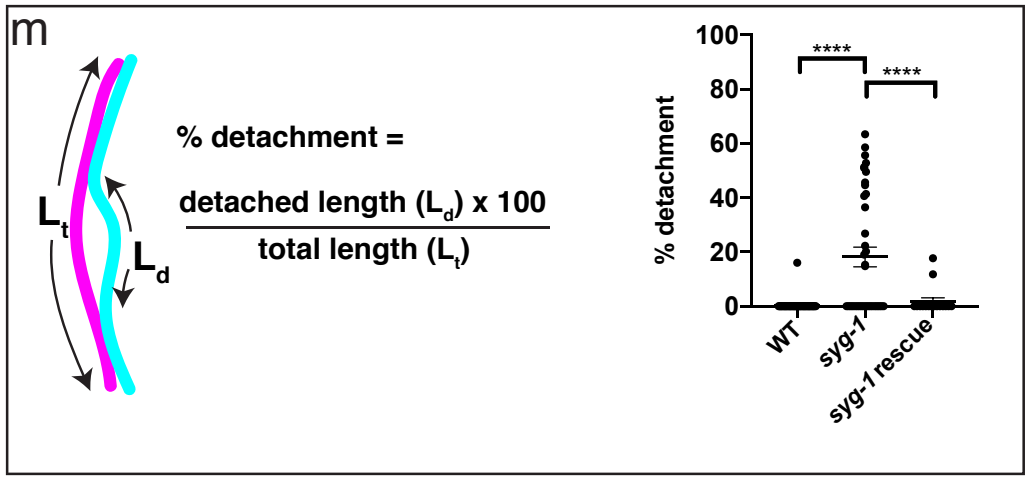
m
L_t
L_d
% detachment =
detached length (L_d) x 100
total length (L_t)
% detachment
100
80
60
40
20
0
****
****
WT
syg-1
syg-1 rescue

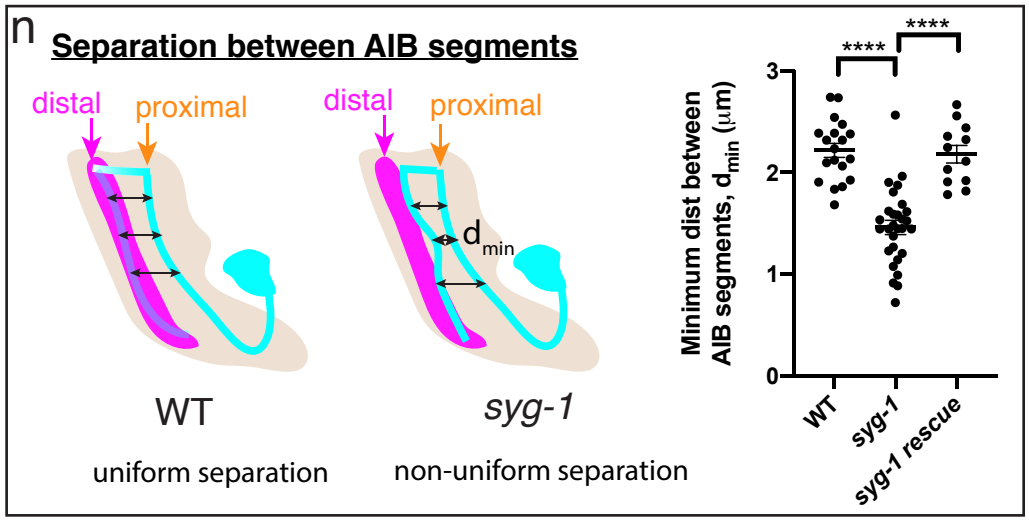
n
Separation between AIB segments
distal
proximal
distal
proximal
d_{min}
WT
syg-1
uniform separation
non-uniform separation
Minimum dist between AIB segments, d_{min} (µm)
3
2
1
0
****
****
WT
syg-1
syg-1 rescue

Figure 4

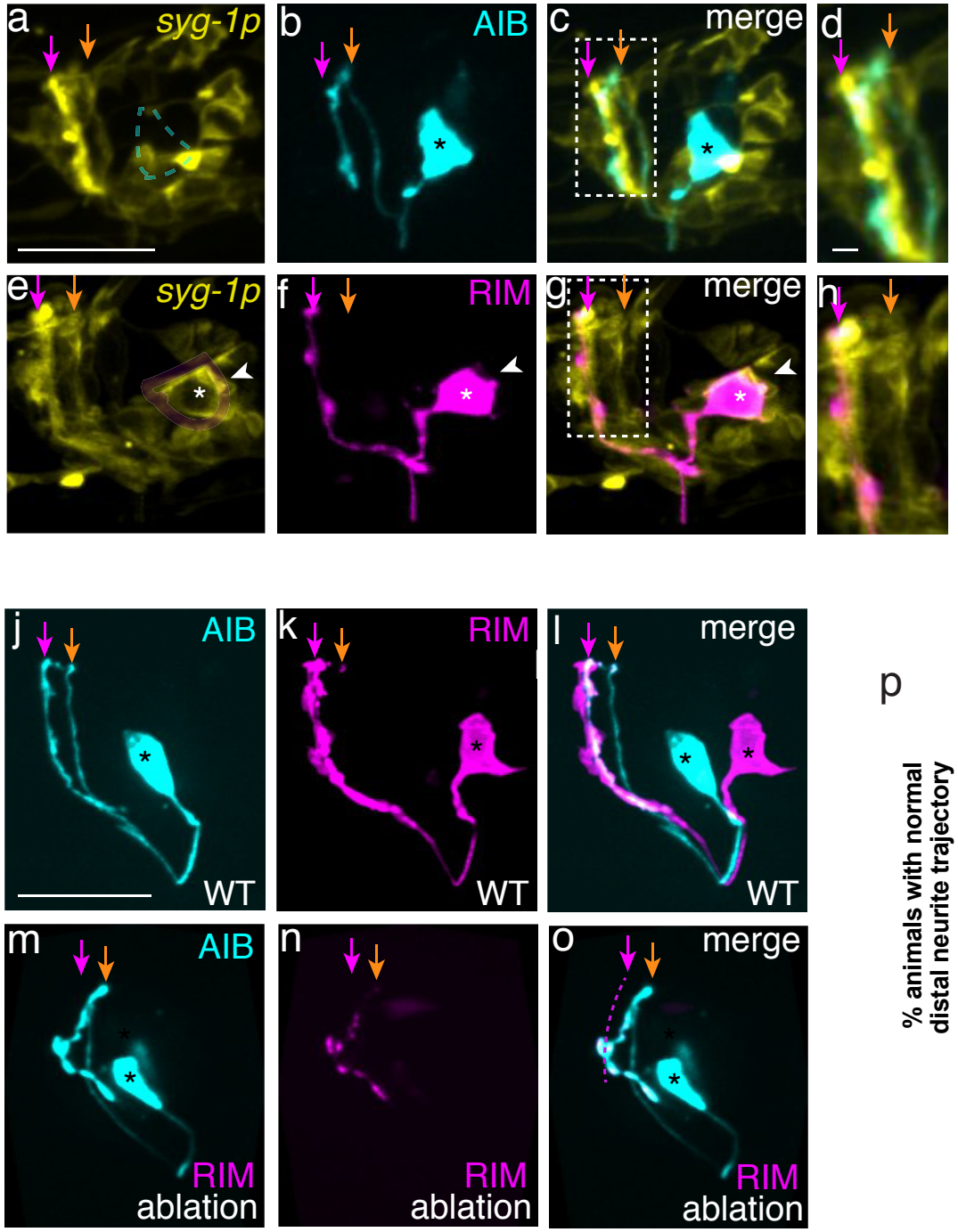
a
syg-1p
b
AIB
c
merge
d
e
syg-1p
f
RIM
g
merge
h
j
AIB
WT
k
RIM
WT
l
merge
WT
m
AIB
RIM
ablation
n
RIM
ablation
o
merge
RIM
ablation

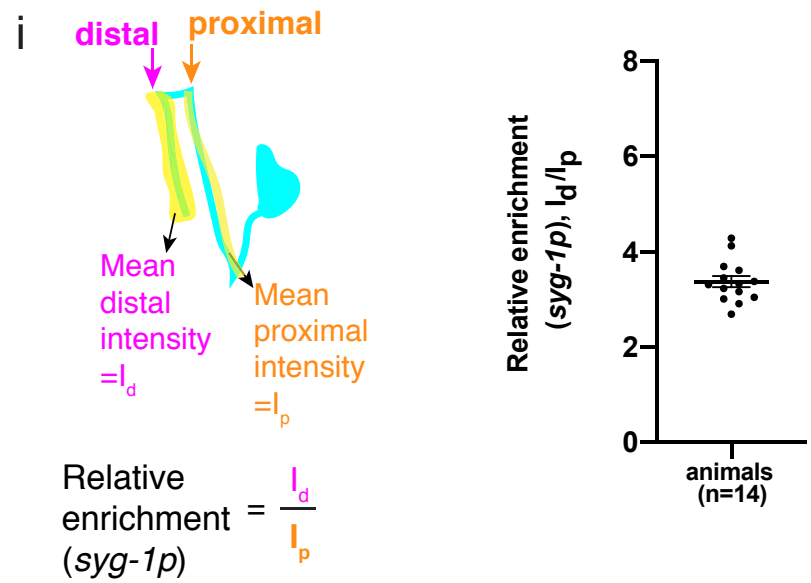
i
distal
proximal
Mean distal intensity =I_d
Mean proximal intensity =I_p
Relative enrichment (syg-1p) = I_d / I_p
Relative enrichment (syg-1p), I_d/I_p
8
6
4
2
0
animals (n=14)

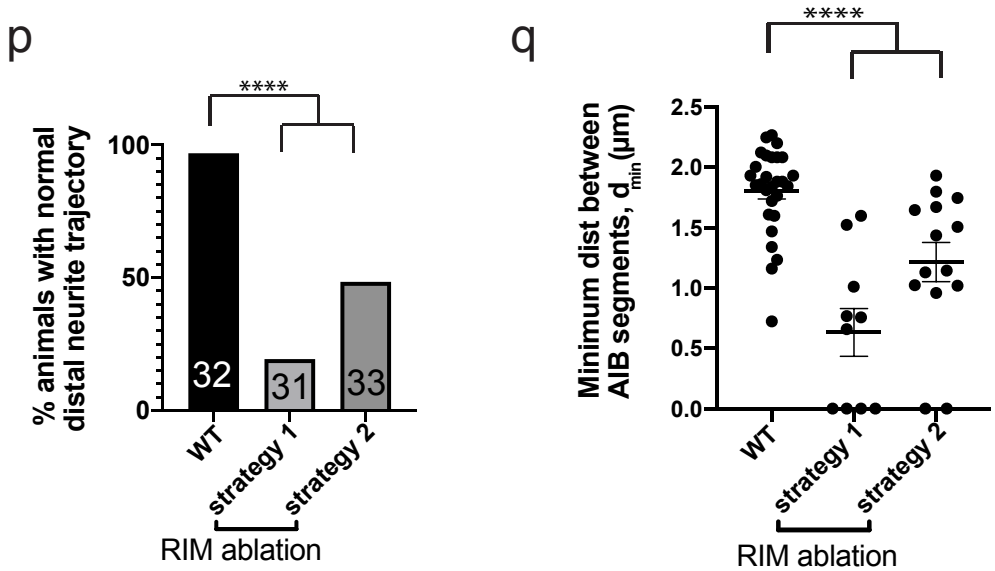
p
****
% animals with normal distal neurite trajectory
100
50
0
32
31
33
WT
strategy 1
strategy 2
RIM ablation
q
****
Minimum dist between AIB segments, d_min (µm)
2.5
2.0
1.5
1.0
0.5
0.0
WT
strategy 1
strategy 2
RIM ablation

Figure 5

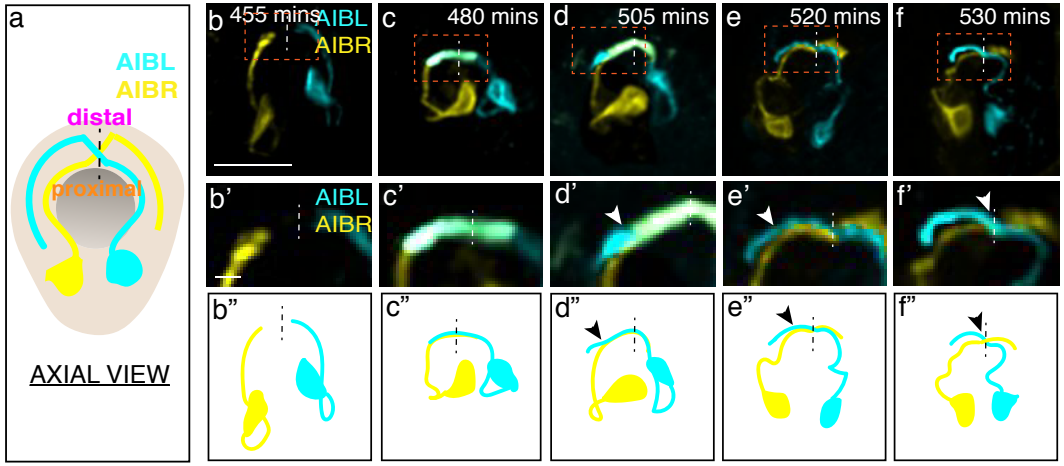
a
AIBL
AIBR
distal
proximal
AXIAL VIEW
b 455 mins
AIBL
AIBR
c 480 mins
d 505 mins
e 520 mins
f 530 mins
b'
c'
d'
e'
f'
b"
c"
d"
e"
f"

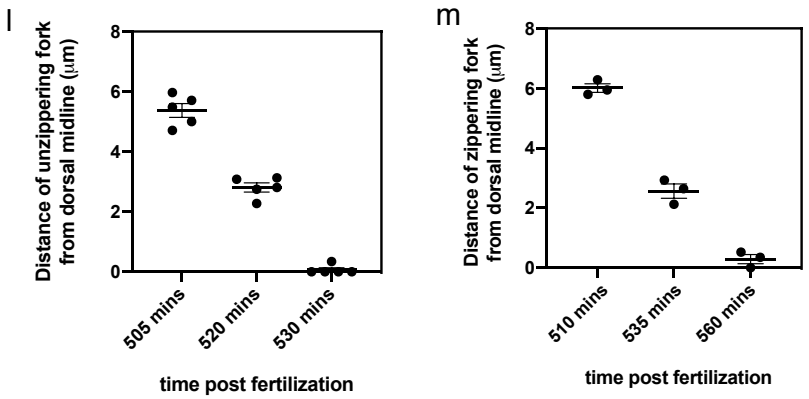
l
Distance of unzippering fork from dorsal midline (µm)
0
2
4
6
8
505 mins
520 mins
530 mins
time post fertilization
m
Distance of zippering fork from dorsal midline (µm)
0
2
4
6
8
510 mins
535 mins
560 mins
time post fertilization

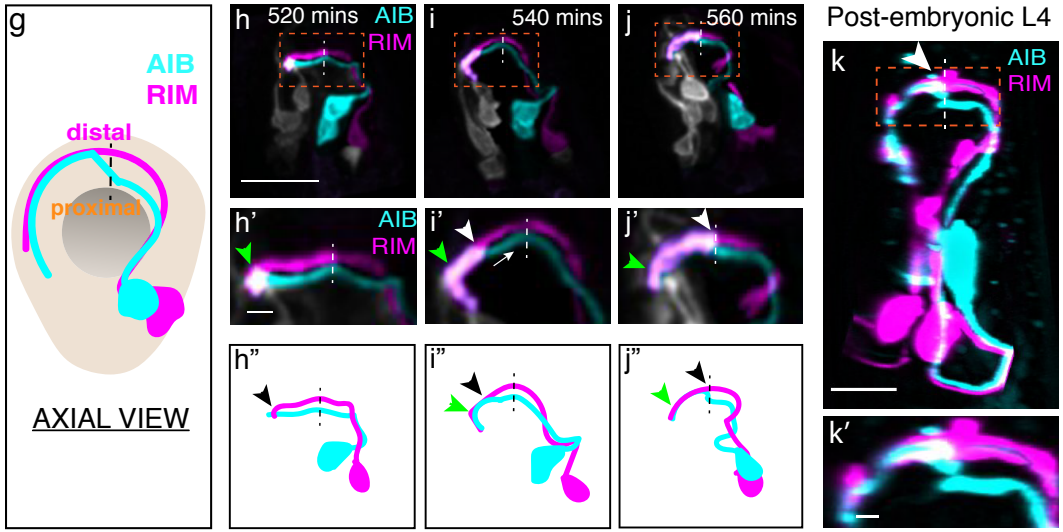
g
AIB
RIM
distal
proximal
AXIAL VIEW
h 520 mins
AIB
RIM
i 540 mins
j 560 mins
h'
i'
j'
h"
i"
j"
Post-embryonic L4
k
AIB
RIM
k'

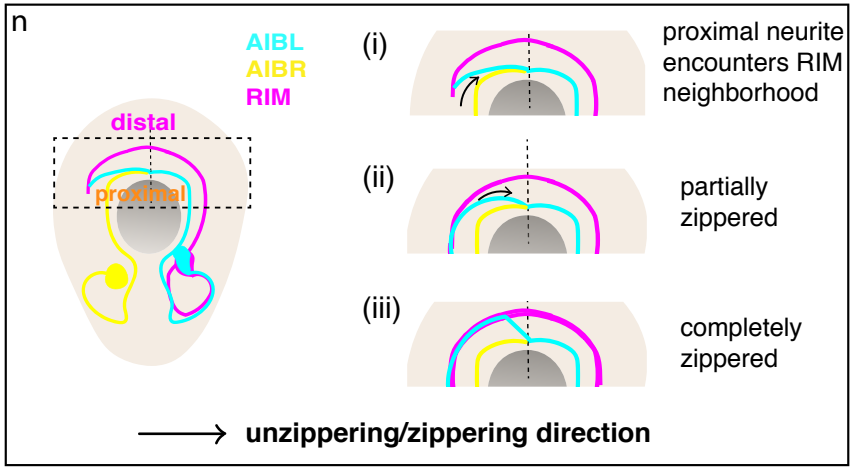
n
AIBL
AIBR
RIM
distal
proximal
(i)
proximal neurite encounters RIM neighborhood
(ii)
partially zippered
(iii)
completely zippered
unzippering/zippering direction

Figure 6

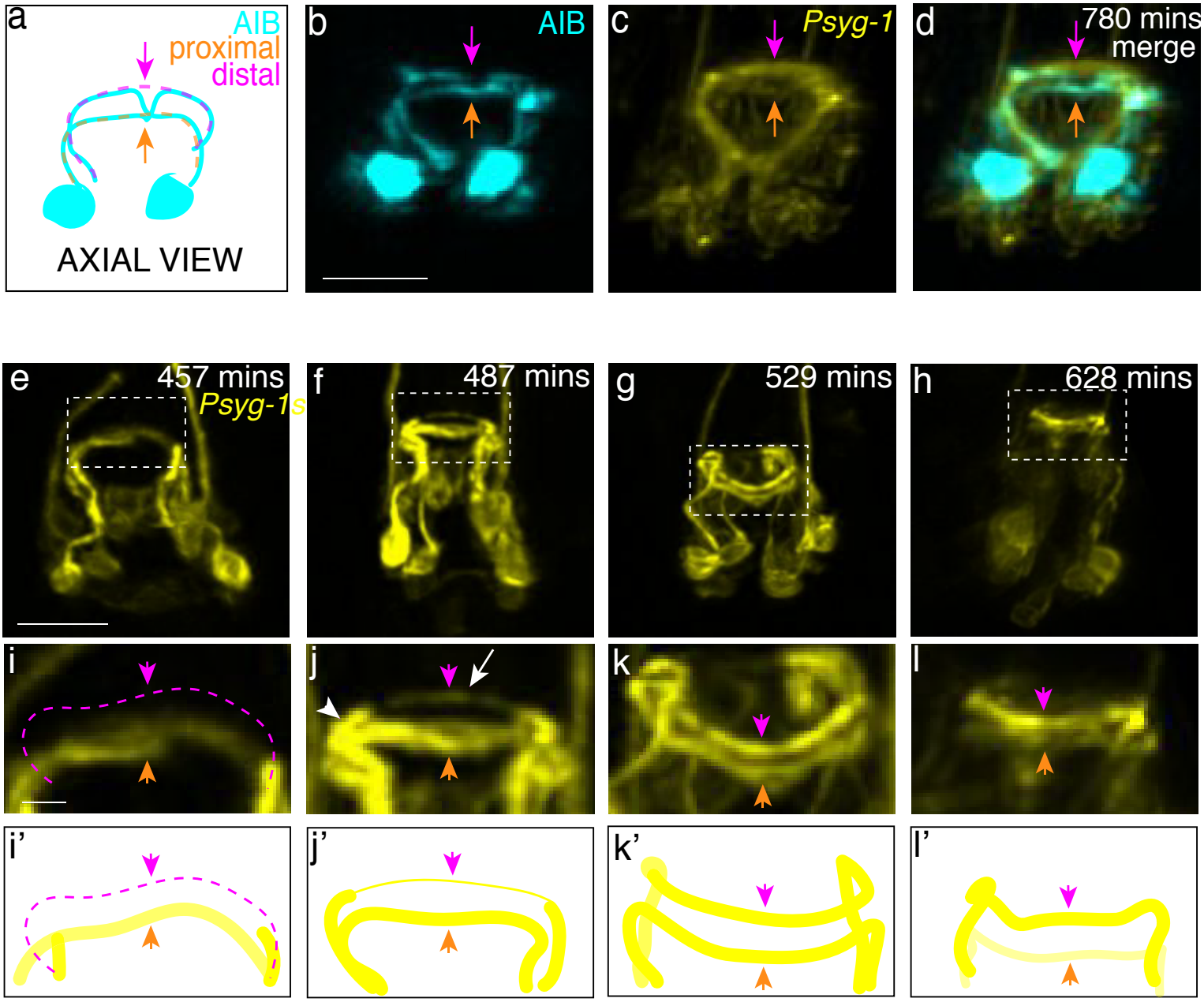
a
AIB
proximal
distal
AXIAL VIEW
b
AIB
c
Psyg-1
d
780 mins
merge
e
457 mins
Psyg-1s
f
487 mins
g
529 mins
h
628 mins
i
j
k
l
i'
j'
k'
l'

Figure 7

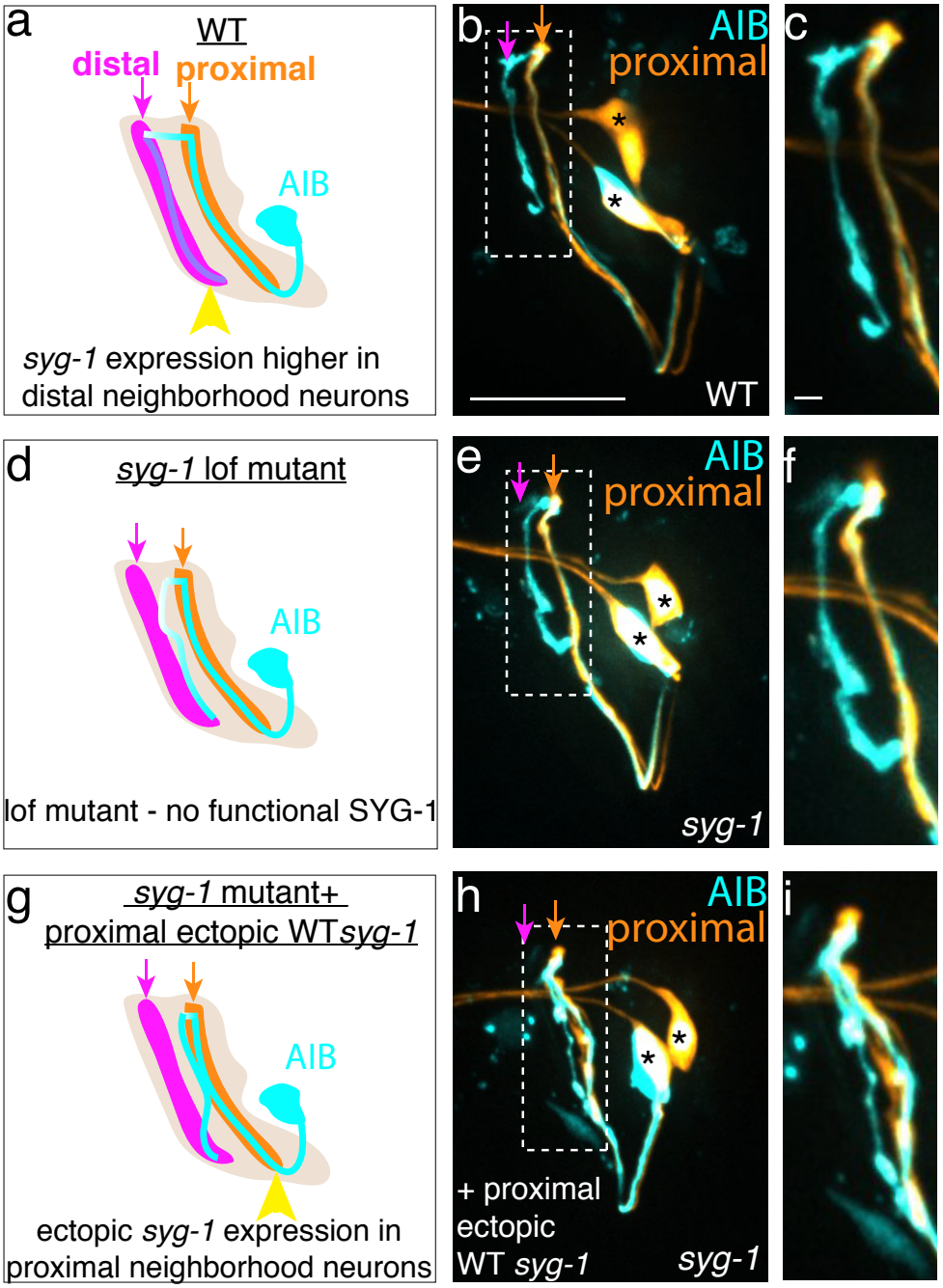
a
WT
distal
proximal
AIB
syg-1 expression higher in distal neighborhood neurons
b
AIB
proximal
WT
c
d
syg-1 lof mutant
AIB
lof mutant - no functional SYG-1
e
AIB
proximal
syg-1
f
g
syg-1 mutant+
proximal ectopic WTsyg-1
AIB
ectopic syg-1 expression in proximal neighborhood neurons
h
AIB
proximal
+ proximal ectopic WT syg-1
syg-1
i

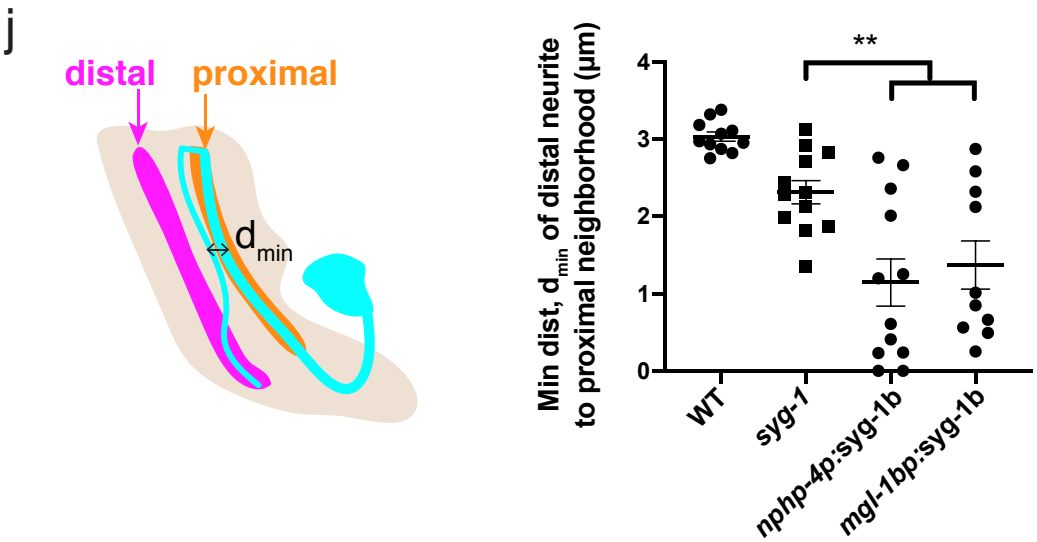
j
distal
proximal
d min
Min dist, d min of distal neurite to proximal neighborhood (µm)
0
1
2
3
4
**
WT
syg-1
nphp-4p:syg-1b
mgl-1bp:syg-1b

Figure 8

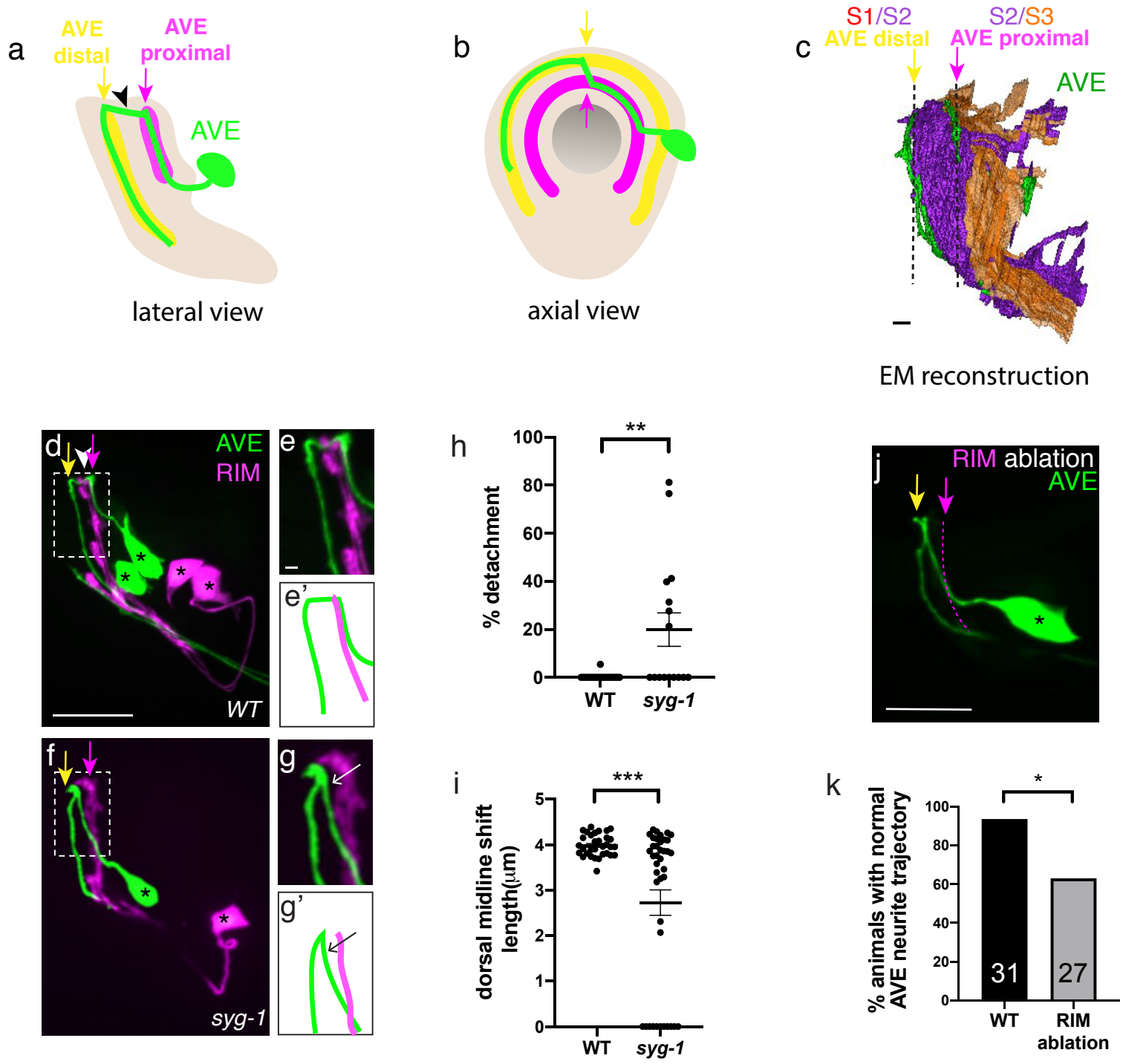
a
AVE distal
AVE proximal
AVE
lateral view
b
axial view
c
S1/S2
AVE distal
S2/S3
AVE proximal
AVE
EM reconstruction
d
AVE
RIM
WT
e
e'
f
syg-1
g
g'
h
% detachment
100
80
60
40
20
0
**
WT
syg-1
i
dorsal midline shift length(μm)
5
4
3
2
1
0
***
WT
syg-1
j
RIM ablation
AVE
k
% animals with normal AVE neurite trajectory
100
80
60
40
20
0
*
31
27
WT
RIM ablation